Review 1

NanoSIMS study of seismically deformed zircon: Evidence of Y, Yb, Ce and P re-distribution and resetting of radiogenic Pb

Elizaveta Kovaleva*[1,2], Urs Klötzli[2]

[1] Geology Department, University of the Free State, 205 Nelson Mandela Drive, 9300 Bloemfontein, South Africa

[2] Department of Lithospheric Research, Faculty of Earth Sciences, Geography and Astronomy, University of Vienna, Althanstrasse 14, A-1090 Vienna, Austria

* Corresponding author. E-mail: kovalevae@ufs.ac.za

Abstract

Lattice defects in zircon can cause trace elements re-distribution and disturbance of isotopic systems. This study investigates in detail how seismically-induced deformation microstructures in zircon correlate with trace element and isotope re-equilibration.

Felsic mylonites with pseudotachylyte veins from the Ivrea-Verbano Zone in Northern Italy were investigated with special focus on deformed zircon. We have revealed the following post-growth deformation microstructures: planar deformation bands (PDBs), planar fractures (PFs), non-planar fractures (both healed and open), and finite strain patterns. PDBs are planar portions of crystal lattice that are strictly parallel to {100} crystallographic planes, and are rotated to up to 3° with respect to the host grain. They are from 0.5 to 1 µm wide and have average spacing of 5 µm. PDBs originate in seismically-active environment at elevated differential stress, strain rate and temperature.

Several grains, in which PDBs are observed, were analyzed with ion microprobe. Ion maps indicate re-distribution of radiogenic Pb isotopes associated with PDB formation. Isotopic re-distribution preferably occurs in PDBs with larger crystallographic misorientation. Profiling demonstrated clear spatial correlation of PDBs with variations of REE abundances (both gain and loss), and possible correlations with increased and decreased Hf, Ti and P abundances. Trace elements can be depleted or enriched (compared to the abundance in surrounding matrix) in deformed domains, depending on the spacing of PDBs and the proximity of the analyzed volume to grain boundary or to detrital core. $^{207}Pb/^{206}Pb$ ratio demonstrates systematic Pb-loss in the PDB-bearing lattice domains with respect to PDB-free domains; in some cases Pb-gain is observed, where the PDBs source radiogenic Pb from older detrital cores.

Our study has important implications for geochronology and microchemistry of zircon from seismically-deformed sections of Ivrea-Verbano Zone and from other paleo-seismic zones of the world. Zircon found in seismically-deformed rocks near pseudotachylyte veins may demonstrate distorted and even reset isotopic ages, and altered trace element abundances. Enhanced trace element exchange between deformed zircon and host mylonite can influence mass balance calculations for the bulk rock.

Keywords: paleo-seismic zones, zircon, planar deformation bands, trace elements, isotopes, geochronology, ion probe

INTRODUCTION

Planar microstructures in zircon

Various planar microstructures are commonly identified in shock-deformed zircon. They include planar deformation features (PDFs) (e.g., Leroux et al. 1999; Timms et al. 2012; Grange et al. 2013; Erickson et al. 2013a), planar fractures (PFs) (e.g., Bohor et al. 1993; Kamo et al. 1996; Kalleson et al. 2009; Cavosie et al. 2010; Moser et al. 2011; Erickson et al. 2013a, 2013b; Thomson et al. 2014), micro-cleavage (Leroux et al. 1999), shock twins or microtwins (e.g., Moser et al. 2011; Timms et al. 2012; Erickson et al. 2013a, 2013b; Thomson et al. 2014; Cavosie et al. 2015a, 2015b), reidite phase transition along certain planes (e.g., Leroux et al. 1999; Cavosie et al. 2015a; Reddy et al. 2015), and planar deformation bands (PDBs) (e.g., Nemchin et al. 2009; Timms et al. 2012).

However, planar microstructures in zircon are rarely documented in seismically-deformed rocks. This might be because they are only visible using specific techniques (e.g., CL, EBSD), and/or are spatially restricted to specific zones in the rock (e.g., ultramylonites surrounding pseudotachylyte veins, Kovaleva et al. 2015). Planar microstructures in zircon from seismic environment were first identified using CL and BSE imaging by Austrheim and Corfu (2009) in zircon from pseudotachylyte vein from the Svarthumlevatnet metagabbro, South-Central Norway. The authors describe grains with one or two sets of PDFs, which have spacing of ~10 µm and are decorated with submicron cavities locally filled with silicates. Some of PDFs are visible in CL as bright and grey 1 µm-thick features. Formation of these structures is considered to be related to seismic activity.

Kovaleva et al. (2015) reported PDBs coexisting with PFs in terrestrial zircons from paleo-seismic zones in Ivrea-Verbano Zone, Northern Italy. Zircon grains with PDBs are mostly found close to pseudotachylyte veins (within ~1 cm distance) in hosting ultramylonites. The PDBs are crystallographically-controlled planar lattice volumes

This is a preprint, the final version is subject to change, of the American Mineralogist (MSA)
Cite as Authors (Year) Title. American Mineralogist, in press.
(DOI will not work until issue is live.) DOI: http://dx.doi.org/10.2138/am-2017-5975

preserving 0.4° to 2.7° misorientation from the host grain. They are 0.3-1 µm wide and have average spacing of 5 µm (Kovaleva et al. 2015). Similar to shock-induced PDBs (Nemchin et al. 2009; Timms et al. 2012), seismic-generated PDBs are usually parallel to {100} crystallographic planes. PDBs are formed by slip along the glide system <100> {010} with misorientation axis parallel to [001]. Their occurrence was documented in specifically oriented grains, with the long axis roughly parallel to the stretching lineation (Kovaleva et al. 2015; also demonstrated in the present study). These authors suggested that PDBs are the result of crystal-plastic deformation and development of parallel low-angle boundaries. The specific geometry of low angle boundaries occurred due to high differential stresses and strain rates generated by seismic events, or coevally with them (Kovaleva et al. 2015). Additionally, formation of PDBs could be facilitated by the elevated temperature conditions in the vicinity of frictional melts (Kovaleva et al. 2015). PDBs differ from the well-known shock-induced PDFs and PFs, yielding high-quality EBSD zircon patterns, and therefore cannot be considered as open structures or amorphous material (e.g., Erickson et al. 2013a). Furthermore, PDFs described from shock-induced zircon usually occupy the {001}, {110}, {112} and {320} crystallographic planes (e.g., Timms et al. 2012), whereas the reports of PDFs occupying {100} are rather rare (Cavosie et al. 2010; Erickson et al. 2013a). As for PDBs, in most cases they occupy the orientation {100}, and only in one case are parallel to {001} (Kovaleva et al. 2015). Interestingly, PDBs parallel to {100} were also reported in other tetragonal accessory minerals analysed by EBSD, including xenotime (Cavosie et al. 2016).

Diffusion mechanisms in zircon

Zircon is comparatively insoluble in melts and fluids and thus is regarded as chemically robust and inert. Under a broad range of geological conditions this mineral can document and preserve multiple crystallization events within a single grain (e.g., Corfu et al. 2003). This is due to low volume diffusion rates of trace cations characteristically incorporated in the zircon crystal lattice (e.g., Cherniak et al. 1997a, 1997b; Hanchar et al. 2001; Cherniak and Watson 2000, 2003, 2007). Preserved sharp growth zones in crystals of various crystallization ages represent direct evidence for very slow volume diffusion of trace elements in this mineral (e.g., Watson and Liang 1995). Extreme conditions, for example, temperatures of melt-bearing magmatic systems (Bea and Montero 2013) are required to induce diffusion of trace elements in zircon.

However, other diffusion mechanisms, which can be effective at lower temperatures, have been identified in zircon. Pb-loss, which leads to younger apparent isotopic ages, has been well documented in natural samples (e.g., Compston et al. 1986; Ashwal et al. 1999), but was not consistent with experimental predictions for volume diffusion (e.g., Geisler et al. 2002). Elevated diffusion rates in zircon at low temperature can be attributed to the effect of self-irradiation that causes metamictization (Cherniak et al. 1991; Cherniak and Watson 2003). Diffusion is especially effective in fluid presence. Fluid-induced diffusion into the radiation-damaged structure can result in distortion of the U-Pb isotopic systems (e.g., Geisler et al. 2001, 2003).

Enhanced diffusion in dry conditions is also attributed to crystal-plastic deformation (Reddy et al. 2006, 2009; Timms et al. 2006, 2011, 2012; Moser et al. 2009, 2011; Flowers et al. 2010; Piazolo et al. 2012, 2016; MacDonald et al. 2013; Kovaleva et al. 2016; Peterman et al. 2016; Reddy et al. 2016). One mechanism, which is proposed to be responsible for trace element re-distribution in plastically-deformed, zircon is “pipe diffusion”, which is caused by dislocations in the crystal lattice (e.g., Piazolo et al. 2016; Reddy et al. 2016). Another mechanism is re-equilibration due to defect's local stress field. It modifies the chemical potentials of the trace elements and attracts trace elements to dislocation cores (e.g., Timms et al. 2006; MacDonald et al. 2013; "capture zone" in Piazolo et al. 2016). Some authors describe deformation-related Pb-loss, which dramatically affects the apparent isotopic ages in zircon. Specifically, Pb-loss was explained by enhanced out-diffusion of radiogenic Pb isotopes via dislocations and other lattice defects (e.g., Moser et al. 2009, 2011; Nemchin et al. 2009; Piazolo et al. 2012; 2016; Timms et al. 2011, 2012; Peterman et al. 2016). Re-distribution of trace elements and disturbance of isotopic systems is different for different lattice distortion patterns (e.g., Piazolo et al. 2012; Kovaleva et al. 2016). In this study we are going to specifically describe the effect of planar deformation bands on trace element and radiogenic isotope abundances.

Trace element and isotope re-distribution caused by planar microstructures in zircon

The effect of planar deformation microstructures on trace element distribution and isotopic systems in zircon is rarely documented. It was suggested that Pb-loss in zircon may be associated with shock-induced planar microstructures. For example, shocked lunar zircon with PDBs (Timms et al. 2012) revealed the strongest U-Pb age resetting that is spatially attributed to a PDB with the largest misorientation relative to the host crystal (Nemchin et al. 2009). This misorientation reached 12° (Timms et al. 2012). Thus younger $^{207}Pb/^{206}Pb$ ages were found to be correlated with an increase of shock-induced lattice rotation in zircon (Nemchin et al. 2009). However, Cavosie et al. (2015b) demonstrated that shock-induced formation of microtwins and crystal-plastic deformation have no significant effect on U-Pb isotopic ages in zircon from Vredefort. The reason for such variation in researchers' results might be the temperature of deformation. Lattice distortion microstructures in zircon, attributed to grains affected by shock pressures without heating (e.g., at a significant distance from the center of impact structure), have negligible effect on the isotopic system (Moser et al. 2011). On the other hand, shock deformation accompanied by high temperatures can lead to significant Pb-loss due to thermally-driven diffusion of Pb along planar and curviplanar microstructures (Moser et al. 2011). Thus, for planar deformation microstructures to cause significant age disturbance, elevated temperatures are required.

There are very few studies of trace element and isotope re-distribution associated with planar microstructures in zircon that are not shock-induced. Austrheim and Corfu (2009) reported lack of U-Pb age disturbance connected with the formation of seismically-induced PDFs in zircon. However, they analyzed deformed grains by thermal ionization mass spectrometry isotopic dilution (ID-TIMS), which averages local effects.

The influence of seismically-induced PDBs on trace elements and isotopic systems behavior in zircon has not been studied previously. PDBs, being a result of lattice distortion via formation of dislocations, may potentially be responsible for trace element re-distribution in zircon crystal lattice. In this study for the first time the behavior of trace elements and Pb isotopes has been investigated in zircon grains with seismically-induced PDBs. We aim to highlight localized effects on trace element abundances and on Pb isotopic system resetting, which may be associated with paleo-seismic deformation. Studying these effects may provide important information for microchemistry and geochronology of zircon from paleo-seismic zones.

SAMPLING LOCALITY AND SAMPLE DESCRIPTION

Samples were collected from mylonitic metapelites from the Ivrea-Verbano zone (IVZ) close to the village Premosello in the Val d'Ossola (northern Italy). A geological map of the sampling locality is presented in Pittarello et al. (2012).

The IVZ consists of a NE-SW trending, steeply dipping sequence of meta-sedimentary and meta-igneous basic rocks, ultrabasic mantle tectonites and a large underplated igneous complex (Brodie and Rutter 1987; Brodie et. al. 1989). The sequence consists of predominant metasedimentary rocks in the SE and prevailing metabasic rocks and strongly depleted metapelites in the NW. Metamorphism increases progressively from amphibolite facies in the SE to granulite facies in the NW (Rutter et al. 2007), and the metamorphic temperatures reach > 900 °C in Val Strona di Omegna (Redler et al. 2012). The IVZ is interpreted as a lower continental crustal section that experienced thinning and high-temperature regional metamorphism during the uppermost Palaeozoic (Rutter et al. 2007; Quick et al. 2009). The IVZ is transected by a network of high-temperature shear zones, which are subparallel to the regional NE-SW elongation direction of the tectonic unit and can be traced for more than 20 km from Anzola (Val d'Ossola) to Forno (Val Strona) (Brodie et al. 1992). Mylonites in the northern part of the Ivrea-Verbano zone were formed under granulite-facies conditions during crustal extension and contemporaneous magmatic underplating between 315 Ma and 270 Ma (Rutter et al. 2007; Quick et al. 2009; Sinigoi et al. 2011; Klötzli et al. 2014). Peak *P-T* conditions of the sampled area are estimated at 1.0-1.2 GPa and 800-900 °C in metagabbro in Val d'Ossola (Pittarello et al. 2012).

Pseudotachylytes are found in mylonitic metagabbros and metapelites deformed under amphibolite to granulite facies metamorphism in the northern part of IVZ (Techmer et al. 1992; Pittarello et al. 2012). The pseudotachylytes were interpreted to have formed coeval with the main deformation of hosting ultramylonites. Their cross-cutting relationships indicate multiple brittle-ductile cycles of deformation that took place in the upper crust at a depth of ~10 km (Pittarello et al. 2008, 2012). The *P-T* estimates of pseudotachylyte emplacement yielded 550-650° C and 0.4-0.6 GPa confining pressure, based on the occurrence of dendritic titanomagnetite and the presence of orthopyroxene in the pseudotachylytic matrix (Pittarello et al. 2012, and references therein).

Samples were collected from two outcrops at Premosello (N 46°00'15.04"/E 08°19'44.11" and N 46°00'23.65"/E 08°19'41.66"); each outcrop reveals tectonically faulted, mylonitized and foliated felsic metasediments, containing ultramylonites and pseudotachylytes. Pseudotachylytes are usually visible by the unaided eye as concordant dark-grey 2-3 mm thick veins, often offset by fractures. They are typically hosted by ultramylonites and reveal mutually-overlapping relationships with them (Pittarello et al. 2012; Kovaleva et al. 2015). Ultramylonitic shear zones in the felsic mylonites appear as 1-2 cm thick dark rock portions extending parallel to the main foliation. The ultramylonites are intensively folded and delimited by subvertical fractures (see Supplementary Material for Kovaleva et al. 2015).

Felsic mylonites represent strongly restitic, dehydrated metasedimentary rocks. They contain 50 to 500 µm sized garnet porphyroblasts, which are surrounded by a fine-grained foliated matrix consisting of alternating plagioclase- and quartz-rich layers, with intercalated biotite-ilmenite layers. Accessory minerals are zircon and monazite. Both pseudotachylytes and ultramylonites in felsic rocks mainly consist of an ultra-fine-grained matrix composed of plagioclase, quartz, biotite and ilmenite, with minor amounts of garnet. Pseudotachylytes are often rimmed by chilled margins composed of single crystal or poly-crystalline garnet porphyroblasts with dendritic morphology, ranging from 5 to 40 µm in size (Austrheim et al. 1996; Austrheim and Corfu 2009; Pittarello et al. 2012; Kovaleva et al. 2015). Garnet chilled margins formed due to late low-temperature (~550° C) crystallization from the melt (Pittarello et al. 2012). Locally, pseudotachylytes preserve needle-shaped fine grains of 1 to 5 µm length in the matrix (Pittarello et al. 2012; Kovaleva et al. 2015). Possibly, these are microlites, resulting from non-equilibrium (re)crystallization of the frictional melt.

Relationships between deformation microstructures in the analyzed zircon

The analyzed samples have undergone a complex tectono-metamorphic history. Based on the cross-cutting relationships of the microstructures, it was suggested that zircon grains in analyzed samples record a minimum of three stages of tectono-metamorphic evolution (Kovaleva et al. 2015, their Fig. 9a): (1) growing of metamorphic rims on detrital cores; (2) fracturing and fracture healing with fluid; (3) formation of fractures with displacements, PDBs and PFs, accompanied by crystal-plastic deformation in a seismically-active environment.

CL-bright metamorphic rims are cross-cut by all deformation features and thus formed prior to the revealed deformation events. Healed fractures of stage (2), where present, are cross-cut by PDBs, PFs and open fractures. Therefore, minor fracturing and subsequent circulation of fluid (stage 2) happened before shearing and seismicity (stage 3). As documented by Pittarello et al. (2012), formation of the preudotachylytes via releasing seismic energy was simultaneous with shearing and formation of ultramylonites in the rocks of the Ivrea-Verbano Zone (stage 3). Thus, planar microstructures and crystal-plastic deformation of zircon were forming simultaneously, accompanied by brittle deformation with fragment displacements due to sudden release of seismic energy. Some of the open fractures are cross-cut by PDBs, indicating that PDBs formed earlier. In other cases PDBs are terminated by open fractures, indicating that fractures, in contrast, are pre-existing. These observations point to the coeval activation of brittle and plastic deformation in the sample during stage (3) (Kovaleva et al. 2015).

ANALYTICAL METHODS AND DATA REPRESENTATION

Sample preparation, scanning electron microscopy (SEM) and cathodoluminescence (CL) imaging

Zircon grains were studied in grain separates embedded in epoxy discs and in polished thin sections. Mineral separates allow analyses of numerous zircon grains in a single sample, and reveal grains of larger sizes (up to 300 µm in diameter). For the epoxy discs zircon grains were extracted from the host rock by the standard procedure involving rock crushing, sieving to the size of ≤ 300 µm, density separation on a Wilfley table, separation in heavy liquids and with a Frantz magnetic separator with subsequent hand picking. Grains were embedded in Körapox 439 epoxy resin, which is suitable for chemical polishing. The same epoxy was used for thin section preparation. Samples were mechanically polished with 0.25 µm diamond paste and subsequently chemically polished with alkaline colloidal silica solution on an active rotary head polishing machine for 4 hours.

Zircons were identified and characterized by secondary electron (SE) and cathodoluminescence (CL) imaging using a FEI Inspect S scanning electron microscope (SEM) equipped with an Everhart-Thornley detector and a Gatan MonoCL system (Faculty of Earth Sciences, Geography and Astronomy, University of Vienna, Austria), or using a Jeol JSM 6490LV SEM coupled with Oxford Inca Energy EDS (Geological Survey of Austria, Vienna, Austria). Host phases were identified qualitatively by composition using energy-dispersive X-ray spectrometry (EDS). CL images were acquired at electron beam conditions of 10 kV accelerating voltage and probe current of 4.5-5.0 nA.

Forescatter electron (FSE) imaging and electron backscatter diffraction (EBSD) mapping

Zircon grains were examined for potential crystal-plastic deformation microstructures using orientation contrast images acquired with a forescatter electron detector (FSD) mounted on the EBSD-tube of a FEI Quanta 3D FEG instrument (Faculty of Earth Sciences, Geography and Astronomy, University of Vienna, Austria), which is equipped with a Schottky field emission electron source. Electron beam settings were at 15 kV accelerating voltage, and a 4 nA probe current using the analytic (high beam current) mode. Stage settings were at 70° tilt and 14-16 mm working distance. After identification of potentially deformed grains based on orientation contrast, EBSD orientation mapping was applied to the selected grain domains. The FEI Quanta 3D FEG instrument is equipped with an EDAX Pegasus Apex 4 system consisting of a Digiview IV EBSD camera and an Apollo XV silicon drift detector for EDX analysis. EDX intensities and EBSD data were collected simultaneously using the OIM data collection software v6.21. Hough parameters were set to a binned pattern size of 140 pixels, a Theta step size of 1° and a Rho-fraction of 74-86%. After applying a 9x9 convolution mask, 3-15 bands with a minimum pattern contrast of 200 and a minimum peak distance of 3-10 pixels in Hough space were used for indexing. At the given settings indexing rates were between 6 and 24 points per second. EBSD maps were obtained from beam scanning in hexagonal grid mode at step sizes of 0.1 – 0.16 µm.

EBSD indexing of zircon raw data yielded > 99.9% indexed pixels due to the high pattern quality, and therefore data cleaning was not required. The EBSD data in form of false color-coded maps (e.g., Fig. 1c) and pole figures (e.g., Fig. 1d) are represented in the sample reference frame Y-Z and plotted using the EDAX OIM v6.2.1 analysis software. FSE and EBSD maps of grains *in situ* (i.e. in thin sections), as well as their pole figures, are oriented with Y vertical and Z horizontal. However, for the grains 03b and 17, X is vertical and Z is horizontal, where X is a direction parallel to lineation, and Z is a direction perpendicular to main foliation. Colors of the false color-coded misorientation maps and corresponding pole figures show the relative angular misorientation of each data point with respect to a user-selected single reference point within the grain (indicated by a white star marker). Local misorientation EBSD map and misorientation axes density contours in inverse pole figure plot (Fig. 1e) were generated with the MTEX toolbox for MATLAB (Bachmann et al. 2010; Bachman et al. 2011; Mainprice et al. 2011). Misorientation axes were calculated using the threshold of misorientation > 1°. EBSD data are given for the selected subareas of interest as indicated by black rectangles (e.g., Figs. 1-2) or in overlaying insets (e.g., Fig. 3) in orientation contrast images.

Nano-scale secondary ion mass spectrometry (NanoSIMS)

Isotope-selective high-sensitive secondary ion mass spectrometry is able to detect low-abundance isotopes of trace elements (ppb) at nm scale spatial resolution (down to 50 nm) in zircon (e.g., Kusiak et al. 2009; Hofmann et al. 2009, 2014; Boehnke et al. 2013; Storm et al. 2014; Bellucci et al. 2016).

All samples were coated with a 30 nm Au layer and analyzed with a Cameca NanoSIMS 50L at Caltech Microanalyses Center, Pasadena, USA. The analytical conditions were similar to those applied for zircon analyses described in Hofmann et al. (2009, 2014). Zircon grains were analyzed for Y, Yb, P, Hf, Ce, Ti, and three radiogenic isotopes of Pb. An O^- primary beam of -8 kV was used to sputter the samples, and positive secondary ions of +8 kV were measured without energy offset using electron multipliers under high mass resolution conditions. Mass resolving power (MRP) achieved during this analytical session was > 4 000.

Mass spectrum scans were examined before data collection to exclude any significant interferences with the masses of interest (see the detail discussion of potential interferences in Hofmann et al. 2009). Two types of zircon analyses were acquired: ion mapping of unknowns, and individual spot analyses on standards and on unknowns. For both types of analyses, the instrument was tuned to generate a probe diameter of ~600 nm from a primary beam diameter of ~650 nm. Detector dead time was on the order of 44 ns. The isotope ^{90}Zr was chosen for normalization of point analyses and ion maps following the technique described in Hofmann et al. (2014). ^{180}Hf was also used to normalize some of the ion maps, as raw ion images showed that ^{180}Hf has a fairly homogeneous distribution in zircon. Normalization is done to demonstrate specific features in trace element abundances.

For individual spot analyses along line profiles, samples were pre-sputtered for 210-360 sec with the primary beam of ~80-90 pA rastering across 1x1 µm or 2x2 µm areas. Data were collected with a primary beam of about 1-3 pA for about 5 minutes. Secondary ion signals were collected in the “Combined Analysis” mode of the NanoSIMS for the following masses: ^{31}P, ^{49}Ti, ^{89}Y, ^{90}Zr, ^{140}Ce, ^{174}Yb, ^{180}Hf, ^{206}Pb, ^{207}Pb and ^{208}Pb. “Combined analyses” means that the eight masses were collected, followed by re-analyzing of the same spot to collect the remaining two masses. All analyzed zircons were subsequently re-examined with the SEM in order to confirm the locations of ion probe craters and mapping regions.

Ion images of eight masses (^{31}P, ^{89}Y, ^{90}Zr, ^{174}Yb, ^{180}Hf, ^{206}Pb, ^{207}Pb and ^{208}Pb) were collected in the “Combined Analysis” mode over areas of 10x10, 15x15 and 20x20 µm. Samples were pre-sputtered with a scanning primary beam of ~80-90 pA across 25x25 µm areas. Each ion map shown in this study represents a combination of 10 individual maps, which may cause a slight blurring of the picture, caused by insignificantly small beam shifts during measurement duration. Qualitative ion image processing was performed using the software Look@NanoSIMS (Polerecky et al. 2012). Due to the low signals (sometimes as low as 1 count per second) and hence large statistical errors, only qualitative results were obtained from the ion images.

The mentioned isotopes for the trace elements P, Ti, Y, Ce, Yb and Pb were selected such that the range of the isotopic masses are possible to resolve with NanoSIMS at a time. These are the common trace elements in zircon that may reach significant concentrations (e.g., Ti, Y, Yb) and are potentially characteristic for zircon forming environment and formation temperature (e.g., Hoskin and Schaltegger 2003; Watson et al. 2006), and thus are important for zircon microchemistry. Three radiogenic isotopes of Pb (^{206}Pb, ^{207}Pb and ^{208}Pb) were chosen for calculating relative ages and to compare the relative ages between domains with differences in total lattice strain and presented microstructures. ^{180}Hf (minor element) was also used for normalization of ion maps, in cases where it reveled homogeneous distribution in raw maps and in ^{180}Hf/^{90}Zr maps. Remarkable robustness and stability of Hf in zircon lattice was demonstrated before (e.g., Halpin et al. 2012), and makes Hf suitable for normalization of trace elements with very low abundances (e.g., Kovaleva et al. 2016). Heavy isotopes such as U and Th were not analyzed with the NanoSIMS. It is not feasible to analyze them simultaneously with the other lighter isotopes selected for analysis.

For correction of Pb isotopes measurement, the measurements of standard zircons Plesovice (Sláma et al. 2008; Frei and Gerdes 2009) and 91500 (Frei and Gerdes 2009) were evaluated before and after sample analyses. Mean U concentration in Plesovice zircon is 755 wt ppm; mean Th concentration is 78 wt ppm; U/Pb ages yielded 337.13±0.37 according to Sláma et al. (2008), and 337.1±0.4 Ma according to Frei and Gerdes (2009). Mean U concentration in 91500 standard zircon is 69 ppm, mean Th is 37 ppm, and the concordant U/Pb age is 1064±4 Ma (Frei and Gerdes 2009). Those NanoSIMS standard analyses that demonstrated sufficiently high intensities and no correlation between Zr, Hf and Pb were selected to calculate a combined mass bias and fractionation correction factor for the $^{207}Pb/^{206}Pb$ ratio (1.016+0.002, 2SD). All Pb isotope measurements were corrected using this correction factor. $^{207}Pb/^{206}Pb$ relative ages were calculated using the toolbox Isoplot 4.15 for Microsoft Excel (Red X® Holdings). No quantitatively correct estimate of the counting error on the individual $^{207}Pb/^{206}Pb$ ratios and the error on the correction factor was done. Therefore, no error-propagation was made for the final $^{207}Pb/^{206}Pb$ age estimates. The error propagation could be neglected because the data presented is qualitative, and should not be taken as quantitative. Each set of compared data (points from each individual grain are compared with each other) is from one analytical run using the same analytical conditions, so all the data have the same uncertainty variation and thus can be intercompared. Considering the counting errors for the reference zircon measurements, an overall error estimate of 5% (2SD) for the final $^{207}Pb/^{206}Pb$ ratios is proposed. However, this error is not propagated into the final $^{207}Pb/^{206}Pb$ ages reported in the Table 1 and is not shown on the respective figures, which show only qualitative estimated values.

For the isotopic ratios for each profile see Appendix Table 1. Uncertainties (σ_{mean}) for each isotopic ratio were calculated as a standard deviation for each individual profile. They are given in the Appendix Table 2, and added to the error bars in the isotopic ratio plots.

RESULTS

Zircon grains in the analyzed samples have diameters of 30 to 100 µm and are hosted by the ultramylonitic matrix, which is mainly composed of fine-grained quartz and plagioclase, and minor amounts of ilmenite and biotite. Zircon is usually rounded, isometric or slightly elongate, with an aspect ratio 1:1-1:2. In the sampled felsic mylonites, 23-29% of all zircon grains are brittlely deformed, whereas 10-11% show preserved crystal-plastic deformation patterns. The abundance of deformed zircon grains in pseudotachylytes and in associated ultramylonites is higher, where 63-72% of all grains show cataclastic deformation microstructures and 19-28% crystal-plastic deformation microstructures, including grains with planar deformation bands. Fracturing, crystal-plastic deformation and formation of PDBs are not mutually exclusive, and very often various microstructures can be observed together in the same grain (e.g., Kovaleva et al. 2015; this publication). Zircon grains with PDBs are usually found within ultramylonites at the contact with pseudotachylytes, or in the mylonitic matrix hosting ultramylonites.

CL imaging

CL imaging of zircon reveals distinct growth features, such as core-mantle structures. Grains 12 and 26 (Figs. 1 and 2) reveal simple core-mantle CL zonation, showing a darker unzoned core and brighter rim (Fig. 1b); or a CL brighter unzoned core surrounded by a darker rim (Fig. 2b). Grain 43 reveals a detrital core with sector zoning with alternating dark and bright sectors, and a homogeneous CL-bright rim (Fig. 3b). Other analyzed grains show an oscillatory-zoned CL-dark detrital core surrounded by a CL-bright zoned metamorphic rim (Figs. 4-7). CL images also show open fractures appearing as dark lines (Figs. 2b; 3b upper right corner, 6b; 7b), which may produce significant offsets of growth zones (Figs. 2b, 6b, 7b). Healed fractures can be traced by the brighter CL signal (Figs. 1b and 4b, arrows), and may also occur as thin dark CL features (Fig. 7b, arrows). No planar features or finite strain patterns were traced in the CL images of analyzed grains.

Orientation imaging and mapping

Forescatter electron imaging reveals orientation contrast within the individual grains and shows the following deformation features in zircon: finite crystal-plastic deformation (e.g., Figs. 1a, 2a, 3a), planar deformation bands (e.g., Figs. 1a, 3a, 4a, 5a, 6a, 7a), planar fractures (e.g., Figs. 3a, 4a) and open or healed non-planar fractures (e.g., Figs. 3a, 4a, 5a). Traces of planar fractures are usually parallel to PDBs (Figs. 3a, 4a). Open non-planar fractures sometimes generate significant relative displacements of the fragments (e.g., Figs. 6a-b, 7a-b). EBSD maps indicate internal lattice rotations of crystal domains and help to reconstruct the orientations of the microstructural elements with respect to crystallographic planes and directions (Figs. 1c-e; 2c-d; 3a, 5a and 6a - insets).

Finite lattice distortion (non-planar) is found in zircon grains from sampled paleo-seismic zone. Lower right domain of grain 12 shows gradual bending of the lattice, illustrated by undulated gradient of orientation contrast (Fig. 1a), and by rotation of orientation in EBSD map with respect to a reference point by about 10° (Fig. 1c). Additionally, crystallographic axes are systematically rotated around the [331] axis (Fig. 1d, small circle). Misorientation axes demonstrate strong clustering close to the [331] direction (Fig. 1e). The boundary of the grain adjacent to the distorted domain is ragged, contrasting with a smooth boundary trace limiting the undistorted domain (Fig. 1a-b).

Lattice distortion was also documented in grain 26 (Fig. 2). EBSD mapping yielded local misorientation with a “chess-board”-like pattern. Lattice rotation reaches more than 3° with respect to a reference point, showing discrete planar features tracing ENE to WSW (Fig. 2c, indicated by a dotted white line). These planar features are parallel to the (010) plane (Fig. 2d). In addition, there is a small lattice rotation of less than 1° across subvertical low-angle boundaries (Fig. 2c, black arrows), which have orientations parallel to the (100) plane (Fig.

2d). A combination of mutually orthogonal deformation features creates the abovementioned "chess-board"-like finite deformation pattern. Misorientation bands (Fig. 2c) observed parallel to the (100), and thus parallel to the subgrain boundaries, also have planar traces. Thus, there are (sub)planar features parallel to both equivalent planes {100}.

Planar deformation bands (PDBs) are visible in orientation contrast images as multiple thin (500-700 nm) lamellae, spaced from 1 (Fig. 7a) to 15 µm (Fig. 5a), and 4-5 µm on average (Fig. 4a). PDBs are reflected by orientation contrast and trace in one (Figs. 4a, 5a, 7a) or two directions (Figs. 1a, 3a, 6a). Typically they do not produce any distortion in CL images (Figs. 1b, 3-7). Sometimes PDBs can be traced across the entire grain (Figs. 1a, 3a, 4a, 5a), or can be delimited by an open fracture (Figs. 6a, 7a). In EBSD maps PDBs appear as thin, linearly tracing lattice portions that are slightly but systematically rotated with respect to the host crystal (e.g., Fig. 3a, inset; see also Kovaleva et al. 2015). EBSD maps of grains 43 (Fig. 3), 80 (Fig. 5) and 03b (Fig. 6) show that the misorientation of PDBs usually reaches 1-1.5° with respect to the host lattice, and does not exceed 3° (e.g., Fig. 2c). The local misorientation of the sites, where orthogonal PDBs intersect, is elevated and higher than of each individual PDB (Fig. 1c, arrows). PDBs are usually parallel to {100} crystallographic planes (Figs. 1d; 2d; 5c; Kovaleva et al. 2015).

Planar fractures (PFs) are associated with, and are parallel to PDBs. For example, in grains 43 (Fig. 3a) and 91 (Fig. 4a), some PDBs are traced by continuous and discrete PFs, which spatially coincide with the PDBs and overlap them (Kovaleva et al. 2015). In our samples PFs occupy one of {100} planes.

Open non-planar fractures are also characteristic for the analyzed set of zircon grains. Grain 26 (Fig. 2) reveals a set of curviplanar fractures that are parallel to the "chess-board" deformation pattern, i.e. form mutually-orthogonal sets subparallel to {100} crystallographic planes (Figs. 2a, c-d). Some zircon grains show open microfractures that displaced fragments and delimited PDBs, e.g., grains 03b (Fig. 6, vertical microfracture and cataclastic zone) and 17 (Fig. 7, subvertical microfracture).

Healed non-planar microfractures revealed in grains 12 (Fig. 1) and 91 (Fig. 4). CL-bright features can be traced in orientation contrast image as trails of pores (Figs. 1a-b, 4a-b, white arrows). Grain 17 (Fig. 7) has a partially-healed fracture reflected by the linear arrangement of pores and dark CL signal, and can be traced across the entire grain from SW to NE (Fig. 7a-b, white arrows). These healed fractures, however, do not affect the distribution of PDBs.

Detail descriptions of orientation contrast and EBSD data of grains 43 (Fig. 3), 91 (Fig. 4), 03b (Fig. 6) and 17 (Fig. 7) are given in Kovaleva et al. (2015). Some SEM and CL data on these grains are duplicated here for the reader's convenience.

Ion microprobe mapping

Mapping or profiling by NanoSIMS across the domains that contain PDBs has been performed in order to study the potential influence of PDBs on the spatial distribution of trace elements in zircon.

The lower portion of zircon grain 26 revealed evidence of crystal-plastic deformation, including formation of discontinuous (sub)planar features (Fig. 2a, c-d). Isotopic mapping was set in this deformed domain. Maps for $^{89}Y/^{180}Hf$ and $^{31}P/^{180}Hf$ document enrichment (relative to the undeformed zircon matrix) associated with an open fracture in the upper right of the ion map (Fig. 2a, e). $^{174}Yb/^{180}Hf$ is slightly depleted along this fracture. No features in the spatial distribution of these elements were observed that could potentially be linked to crystal-plastic deformation microstructures. Added ^{206}Pb, ^{207}Pb and ^{208}Pb normalized to ^{180}Hf and presented in logarithmic scale reveal elevated abundance relative to the surrounding matrix along the open fracture in the upper right (Fig. 2e). Additionally, Pb isotopes are inhomogeneously distributed, being comparatively enriched between the planar bands, thus forming patchy distribution patterns (Fig. 2e, white arrows).

Ion maps of grain 43 $^{89}Y/^{180}Hf$, $^{174}Yb/^{180}Hf$, $^{31}P/^{180}Hf$ and added counts of Pb, normalized to ^{180}Hf and presented in logarithmic scale, demonstrate enrichment in the CL-dark core domain (Fig. 3b-c), whereas raw map of ^{180}Hf reveals uniform distribution. Added counts of ^{206}Pb, ^{207}Pb and ^{208}Pb normalized to ^{180}Hf are enriched (relative to the surrounding zircon matrix) in the spot at the boundary between CL-dark core and CL-bright rim, where this boundary is intersected by a NW-SE-trending PDB trace (Fig. 3c, white arrow), and close to the spot where two orthogonal sets of PDBs intersect each other, as indicated in the scheme (Fig. 3c, inset). The low counting (0.5 counts per second) of added Pb isotopes are within the noise, thus this Pb cluster might be insignificant. However, consistency in Pb isotopes behavior (enrichment in the same spot) suggests that this is probably a true feature.

Ion maps of grain 91 $^{89}Y/^{90}Zr$ and $^{174}Yb/^{90}Zr$ reveal growth zoning features displayed by CL contrast (Fig. 4b-c). Trace element abundances are elevated compared to surrounding zircon matrix in the CL-dark detrital core (upper part of the chemical distribution maps, Fig. 4b-c). $^{89}Y/^{90}Zr$, $^{174}Yb/^{90}Zr$ and $^{31}P/^{90}Zr$ are also slightly enriched in the lower left part of the map, reflecting faint dark growth zone in the CL-bright rim (Fig. 4b, inset). Furthermore, $^{89}Y/^{90}Zr$ and $^{174}Yb/^{90}Zr$ are slightly enriched (relative to the surrounding zircon) along the healed fracture in the rim, and depleted along the same fracture in the core, while $^{31}P/^{90}Zr$ is slightly depleted along the entire fracture (Fig. 4, white arrows). Added counts of Pb normalized to ^{90}Zr do not reveal any features, probably because the radiogenic Pb abundance is very low (Fig. 4c). ^{49}Ti/^{90}Zr map is also featureless (Fig. 4c).

Ion microprobe analyses

The relative ^{207}Pb/^{206}Pb ages shown in this study do not represent absolute age values. We have used corrected ^{207}Pb/^{206}Pb isotopic ratios in order to estimate the qualitative difference between the ages along the NanoSIMS profiles. Relative ^{207}Pb/^{206}Pb ages are represented as an absolute age difference between each data-point and a reference point that is selected in the least deformed analyzed portion of the grain (Table 1). All points are color-coded according to the age difference with the reference point and are superimposed on top of orientation contrast images (Figs. 5-7).

The ion microprobe profile in grain 80 (fig. 5) was collected within the CL-bright metamorphic rim, across two PDBs documented by orientation mapping (Fig. 5a). The profile was positioned within a single growth zone with almost homogeneous CL intensity (CL bright growth zone), to avoid significant variations of trace element contents. The PDB-bearing grain portions were measured at points 2-3 and 6-7 of the profile (grey shaded area in Fig 5d). Ratios for ^{89}Y/^{90}Zr, ^{174}Yb/^{90}Zr and ^{140}Ce/^{90}Zr decrease at the sites of intersections with PDBs, generating a W-shaped profile (Fig. 5d). ^{180}Hf/^{90}Zr and ^{31}P/^{90}Zr ratios do not show any systematic correlation with PDBs. ^{49}Ti/^{90}Zr is slightly enriched in the domain cross-cut by the upper PDB, and slightly depleted (relative to undeformed domain) in the domain deformed by the lower PDB. ^{206}Pb/^{90}Zr, ^{207}Pb/^{90}Zr and ^{208}Pb/^{90}Zr do not show spatial correlation with PDBs (Fig. 5d). Relative ^{207}Pb/^{206}Pb ages show isotopic resetting in the area of upper PDB, and older comparative ages in lower PDB area (with respect to the reference point 1).

For grains 03b and 17 the spacing of PDBs is smaller than the ion microprobe spot (~1 µm in grain 17, Fig. 7a), therefore, for these samples we describe “PDB-bearing” and “PDB-free” domains, rather than domains intersected by individual PDBs. Grain 03b (Fig. 6) is fractured into two fragments, one of which hosts two sets of PDBs whereas the other does not contain any PDB (Fig. 6a). Ion probe analysis points were positioned in both fragments along the same growth zone in the CL-bright rim (Fig. 6a-b), in order to compare the behavior of trace elements depending on presence of PDBs. Points 1 and 2 were positioned in the PDB-free fragment, whereas points 3-5 were positioned in the PDB bearing fragment. $^{89}Y/^{90}Zr$, $^{174}Yb/^{90}Zr$, $^{180}Hf/^{90}Zr$ and $^{31}P/^{90}Zr$ ratios are elevated in the PDB-bearing domain, and $^{140}Ce/^{90}Zr$ is partially elevated (Fig. 6c). $^{206}Pb/^{90}Zr$, $^{207}Pb/^{90}Zr$, $^{208}Pb/^{90}Zr$ and $^{49}Ti/^{90}Zr$ do not correlate with the presence of PDBs, and are elevated in point 3, which was taken close to the detrital core and to a microfracture (Fig. 6a-c). Relative $^{207}Pb/^{206}Pb$ apparent ages of points 4-5 are younger with respect to the points 1-2, indicating loss and resetting of radiogenic Pb. Point 3 that is set close to the detrital core and microfracture is, in contrast, older in apparent age.

Grain 17 (Fig. 7) is fragmented in two parts, one of which bears PDBs (left in Fig 7a-b), whereas the other is PDB-free (Fig. 7a). Microprobe analyses were taken in one zone along the homogeneous metamorphic rim in both fragments; points 1-2 are taken in PDB-free fragment, and points 3-5 are taken in PDB-bearing fragment (Fig. 7a-b). $^{89}Y/^{90}Zr$, $^{174}Yb/^{90}Zr$, and $^{140}Ce/^{90}Zr$ ratios are slightly decreased in the PDB-bearing domain. $^{180}Hf/^{90}Zr$ ratio is partially decreased. $^{206}Pb/^{90}Zr$, $^{207}Pb/^{90}Zr$, $^{208}Pb/^{90}Zr$ and $^{31}P/^{90}Zr$ do not show any significant correlation; $^{49}Ti/^{90}Zr$ is slightly increased in the PDB-bearing domain (Fig. 7c). Relative $^{207}Pb/^{206}Pb$ apparent ages are younger in the PDB-bearing fragment, with respect to point 1.

DISCUSSION

Planar deformation bands

Formation of PDBs in our samples was simultaneous to mylonitization and crystal-plastic deformation during seismic activity of the unit (evolution stage 3). This can be shown with grain 12 (Fig. 1). In this zircon we observe lattice bending that have overlapping relationships with PDBs in the lower right domain of the grain (Fig. 1a, c). Ragged grain boundary adjacent to the strained domain is evidence of dissolution. Dissolution may be enhanced by crystal-plastic deformation, as the increased defect density results in increased surface reactivity. Ragged boundary may also be a result of marginal grain size reduction, which is a part of mylonitization process (e.g., Kovaleva et al. 2014).

Planar deformation bands, as well as lattice bending (Fig. 1a, c) and low angle boundaries (Fig. 2c), are the result of crystal-plastic deformation. We suggest that the discrete (sub)planar deformation microstructures in grain 26 (Fig. 2) are the remnants of planar deformation bands. These deformation microstructures are parallel to zircon {100} planes. Such orientation is characteristic for PDBs. One of these (sub)planar bands traces into the offset fragment (Fig. 2a, pointed by the white arrow). Moreover, the host grain has the orientation, preferable for PDBs formation with the <c> axis parallel to the mylonitic lineation (Fig. 2d). The discrete nature of these planar features can be caused by the formation of overlapping, orthogonal set of low-angle boundaries (Fig. 2c, arrows) that occurred during superimposed crystal-plastic deformation. Moreover, finite deformation structures are overlapped and distorted by the orthogonal set of curviplanar fractures that are stretching in the same directions subparallel to {100} crystallographic planes (Fig. 2a). Fracturing could be facilitated by the pre-existing lattice distortions (PDBs and low-angle boundaries) and occurred shortly after crystal-plastic deformation during the evolution of the rock stage (3). PDBs might have been also distorted and partially erased due to annealing in the vicinity of frictional melt.

Microstructures and textures in zircon that affect trace element distribution

Ion probe mapping resolved inhomogeneities in trace element abundances, spatially connected with various growth and deformation features, such as growth zoning (Figs. 3c, 4c), healed fractures (Fig. 4c), open fractures (Fig. 2e), and PDBs (Figs. 2e; 3c).

Variations in trace elements abundance due to *growth zoning* are fairly pronounced in the ion maps. Grains 43 and 91 reveal CL-dark oscillatory zoned detrital cores that are rich in ^{89}Y, ^{174}Yb and ^{31}P, in contrast with the CL-bright metamorphic rims (Figs. 3c, 4c). The correlation between CL-dark zones and increased REE abundance is described, for example, in Cavosie et al. (2006). Their SIMS analyses of a strongly zoned zircon demonstrated that the CL-dark sectors contain elevated trace element abundance as compared to the CL-bright sectors. Elevated concentration of Y in CL-dark zones has been also documented by Nasdala et al. (2010). Our results are also partially consistent with the results derived by Hofmann et al. (2009, 2014), who demonstrated that CL-dark oscillatory zones in zircon are in most cases correspond to elevated concentrations of ^{89}Y, ^{49}Ti, ^{140}Ce and ^{31}P. However, we did not document elevated ^{49}Ti abundance in the CL-dark zones. ^{49}Ti remains homogeneous across detrital core and metamorphic rim (Fig. 4c). Such Ti behavior is not completely inconsistent with the result of Hofmann et al. (2014), who documented a common spatial correlation between abundances of Ti and other trace elements (specifically P, Y and Ce) in magmatic zircon. Isotopes of Pb are also slightly elevated in the detrital cores (Fig. 3c), which may be evidence of the older isotopic age of the core. Slight elevations in ^{89}Y, ^{174}Yb and ^{31}P are also observed in grain 91, in the lower left corner of the ion map (Fig. 4c). This is consistent with faint dark growth zone in the metamorphic rim. Variations of trace element abundances along the growth zoning can be explained by non-equilibrium crystallization and the specifics of the kinetic mechanisms operating at the crystal/melt (fluid) interface (Hoskin and Schaltegger 2003; Hofmann et al. 2009).

The other group of features that controls trace element distribution in zircon is various *deformation microstructures*, which have significant influence on zircon microchemistry as post-growth effects. Ion mapping documented a *healed fracture* in grain 91 (Fig. 4, white arrows), that is characterized by elevated ^{89}Y and ^{174}Yb abundances in the metamorphic rim, and decreased abundances of the same trace elements in the CL-dark core (Fig. 4c). ^{31}P is depleted along that fracture in both rim and core. Such specific REE abundance may be explained by the composition of the healing Zr-saturated fluid and fluid-mineral diffusional exchange between the fluid and the zircon grain along the fracture (Rimsa et al. 2007). The Zr-saturated fluid that healed the fracture was depleted in HREE content compared with the detrital core, and, in contrast, enriched in HREE compared to the metamorphic rim. Such diffusional exchange should be possible at the granulite-facies conditions of the deformation. The bright CL response of the healed fracture might be caused by elevated LREE elements in the new zircon (Rimsa et al. 2007). P depletion in the fracture may be evidence of the absence of the xenotime-type substitution during healing.

Open fracture in grain 26 is about 1 µm in width (Fig. 2a) and enriched in ^{89}Y and ^{31}P. Microfracture in grain 03b is less than 0.5 µm in width (Fig. 6a) and enriched in ^{89}Y, ^{174}Yb, ^{49}Ti and ^{31}P. ^{89}Y, ^{49}Ti, ^{140}Ce and ^{31}P increased abundances were described before along open fractures in zircon analyzed by Hofmann et al. (2009). Such enrichment is explained either by later hydrothermal precipitation of zircon along the fractures, or by a trace element exchange between fracture wall and the metamorphic fluid (Hofmann et al. 2009).This depletion might also be due to sputtering effects associate with the fracture. Fractures in both analyzed grains (26 and 03b) are enriched in radiogenic Pb (Figs. 2e; 6c), which could be due to the Pb contamination from the matrix. On the other hand, for the grain 03b (point 3) radiogenic isotopes enrichment and Pb-gain effects may be connected with the proximity of the CL-dark core (Fig. 6b).

The effect of PDBs on trace element abundances

Deformation microstructures in zircon may act as fluid migration and fast element-diffusion pathways that cause local variations in the chemical and isotopic composition of grains (Timms et al. 2006, 2011; Piazolo et al. 2016; Reddy et al. 2016). PDBs are the result of crystal-plastic deformation and are forming by dislocation creep along commonly reported slip system in zircon <100> {010} (Kovaleva et al. 2015). Therefore, the formation of PDBs may cause re-distribution of trace elements in the distorted lattice domains. We expect PDBs to affect microchemistry not locally, but in large volumes of zircon lattice (i.e. the whole grain), because they usually extend through the entire grains (e.g., Figs. 1a, 3a), cross-cutting both detrital cores and metamorphic rims (e.g., Figs. 3a-b, 4a-b, 5a-b). Thus cores and rims of individual zircon grains with PDBs may exchange trace element orders of magnitude faster than via volume diffusion.

Consistently, some of the PDBs reveal a slight effect on zircon microchemistry, mostly on Pb isotopes. Pb isotope re-distribution is observed in zircon grain 26, where they form enriched clusters ranging from 1 to 1.5 µm in diameter (Fig. 2e, arrow). The presence of micrometer-scale clusters of Pb isotopes is consistent with the chess-board finite lattice distortion pattern formed by PDBs and orthogonal sets of low-angle boundaries. Pb-enriched clusters are spotted between planar microstructures, therefore, the latter may have experienced Pb-loss, when the surrounding matrix experienced Pb-gain. Inhomogeneous distribution of Pb is not uncommon in deformed and metamorphosed zircon. Valley et al. (2014), Kusiak et al. (2013, 2015), Peterman et al. (2016) and Piazolo et al. (2016) have demonstrated a highly-inhomogeneous distribution of radiogenic Pb isotopes in zircon lattice at a very high spatial resolution (10-20 nm-scale). "Patchy" distribution of Pb is a result of migration of lead in response to (poly)-metamorphism (Kusiak et al. 2013). Our results are consistent with those of Piazolo et al. (2016), who observed numerous Pb-enriched clusters next to low-angle boundary.

Another example of inhomogeneous distribution of Pb isotopes is observed in grain 43 (Fig. 3). An enriched spot approximately 1.5 μm in diameter spatially corresponds to the intersection of two orthogonal PDBs and the boundary between CL-dark core and CL-bright rim (Fig. 3c, arrows, inset). We have demonstrated that the misorientation angle of deformed lattice is increased at the sites of PDBs mutual intersection (Fig. 1c). In turn, elevated misorientation means higher dislocation density. Peterman et al. (2016) has shown that radiogenic Pb can be trapped and moved by dislocation loops due to increased temperatures associated with metamorphism, forming toroid-shaped clusters. Thus dislocations that form PDBs may cause and enhance mobilization and re-distribution of radiogenic Pb. Radiogenic Pb in analyzed sample may be moved from the older core towards the younger rim and accumulate at the site of PDBs mutual intersection, being trapped in domain with high dislocation density. Such Pb re-distribution may cause isotopic age disturbances in the core and rim. If a significant amount of Pb is transported from the older core to the younger rim via PDB networks, the measured ages of the rim can be increased. According to Peterman et al. (2016) and Piazolo et al. (2016), radiogenic Pb clusters mark the timing of metamorphism/deformation (Peterman et al. 2016).

The most pronounced Pb re-distributions are associated with the PDBs with the greatest angular misorientation with respect to the host lattice. Misorientation in grain 26 reaches a maximum of 3° with respect to the unstrained host lattice (Fig. 2c); and the thickness of PDBs is about 1-1.5 µm. Re-distribution of Pb in this grain is fairly pronounced. Smaller misorientations and thicknesses of PDBs, observed in grain 43 (1-1.5° and 500-700 nm, Kovaleva et al. 2015; Fig. 3), cause less disturbance in Pb distribution. No EBSD data was obtained from grain 91 (Fig. 4), so the misorientation degrees of PBDs are not known. Nevertheless, no Pb disturbance was observed in the mapped domain of grain 91. The phenomenon has been described by Nemchin et al. (2009) and Timms et al. (2012) in lunar zircon with PDBs. Abovementioned authors have noted that the PDBs high in misorientation produce significant U-Pb resetting. Moser et al. (2011) has also documented that the domain of maximum crystallographic misorientation spatially coincides with the area of maximum Pb-loss in zircon. High misorientation evidences of larger amount of dislocations accumulated along the PDBs, which hence would cause higher degree of Pb-loss and resetting of the isotopic ages.

Evidence of trace element re-distribution by PDBs has been documented by ion probe profiles, even for PDBs with comparatively low misorientation of about 1° (e.g., Fig. 5a). In grain 80 $^{89}Y/^{90}Zr$, $^{174}Yb/^{90}Zr$ and $^{140}Ce/^{90}Zr$ ratios show decreased values where the profile intersects PDBs (Fig. 5). This may be evidence of Y and Yb transport from the affected lattice domains through PDBs via associated dislocations. Other trace elements are re-distributed, but do not show consistent behavior. They are either removed or added through PDBs to the affected lattice domains. For example, $^{49}Ti/^{90}Zr$ ratio decreases across the upper PDB (points 2-3) and increases across the lower PDB (points 6-7). The upper analyzed PDB cuts through metamorphic rim without cutting through the detrital core. In contrast, the lower PDB cuts through the CL-dark core. Elevated Ti abundance in points 6-7 shows that Ti might be derived from the higher-Ti detrital core through lower PDB. Harrison and Schmitt (2007) showed that elevated Ti abundance in certain zircon domains (and, therefore, elevated temperatures derived from Ti-in-zircon thermometer) can occur due to Ti inward-diffusion through lattice defects. Such explanation is consistent with our results and may be applied to the other trace element abundances, in order to explain inconsistency in their distribution. Trace elements can be sourced from the CL-dark trace-element enriched detrital core. In grains 03b and 17 (Figs. 6-7) PDBs have particularly small spacing, thus we have compared the results gained from affected and unaffected domains of each grain. The results of ion profiling for these two grains appear to be the opposite: grain 03b shows enrichment in $^{89}Y/^{90}Zr$, $^{174}Yb/^{90}Zr$, $^{140}Ce/^{90}Zr$, $^{180}Hf/^{90}Zr$, and $^{31}P/^{90}Zr$ ratios in the PDB-bearing domain with respect to PDB-free (Fig. 6c). In contrast, grain 17 demonstrates the same ratios to decrease in PDB-bearing domain with respect to PDB-free (Fig. 7c). There may be two not mutually exclusive possibilities to explain such inconsistency. On one hand, points 4-5 in grain 03b were analyzed close to the grain boundary (< 5 µm distance), and point 3 was set close to the fracture (Fig. 6a), where the deformed lattice may gain trace elements from an external source via dislocations (e.g., Timms et al. 2006, 2011). Whereas analyses of grain 17 were made at a larger distance from the grain boundary (≥15 µm, Fig. 7a), so the trace elements were removed via dislocations and not gained from the external source. On the other hand, PDBs in grain 17 are more frequent and have smaller spacing than in grain 03b. Therefore, they should be more efficient in removing trace elements from the deformed crystal lattice.

To conclude our results, the ion mapping shows that PDBs can affect spatial distribution of radiogenic Pb isotopes (Figs. 1e; 3c). The ion probe profiling demonstrates that PDBs can affect not only Pb distribution, but also Y, Yb, P, Ce, and, possibly, Ti and Hf. For this specific analytical session and chosen conditions, ion mapping seems to be less effective in documenting trace element re-distribution via PDBs than ion profiling. We suggest that PDBs are so extensive, that they affect larger lattice domains than accessible by the spatial resolution of mapping, and cause grain-scale re-distribution of trace elements. Point analyses and profiles covered much wider areas in analyzed grains and were able to show the trace element re-distribution at a larger scale. Additionally, lattice volume analyzed by the ion probe profiling is more substantial than the volume analyzed by mapping.

PDBs often cross-cut the whole grain or large grain domains, and thus may facilitate trace element diffusion at the grain scale inwards and outwards of the affected grain or domain. Reddy et al. (2006) and Timms et al. (2006, 2011) discussed the potential influx of REE, Th and U via deformation microstructures towards the interior of zircon grains. Ti- and Pb-depletion in low-angle boundaries has been found by Timms et al. (2011). MacDonald et al. (2013) have also documented decreased Ti-content from distorted grains. Consistent with the abovementioned studies, we observe both gain and loss of REE, Hf, P and Ti, depending on location; and Pb-loss in all cases. Taking into account the possible effect of PDBs on Ti (Figs. 5, 7), we suggest that these microstructures may produce disturbances of the Ti-in-zircon thermometer, resulting in both higher- and lower-temperatures (e.g., Harrison and Schmitt 2007; Timms et al. 2011; Kovaleva et al. 2016). Ti might be gained from the mylonitized matrix, rich in ilmenite. The potential effect of PDBs on P distribution (Figs. 5-7) can influence the xenotime-type substitution mechanism ($(Y, REE)^{3+} + P^{5+} = Zr^{4+} + Si^{4+}$), and thus affect the dependence of xenotime solubility in deformed zircon lattice (e.g., Hoskin and Schaltegger 2003; Reddy et al. 2016). In 03b (Fig. 6) the P abundance mimics that of Y and Yb, which can indicate coupling between P and REE, leading to a xenotime-type substitution. Abundances of all three elements are elevated in PDB-bearing domain (Fig. 6c), thus presence of PDBs possibly enhances the ability of xenotime to dissolve in zircon (Reddy et al. 2016).

Grains 91 and 80 (Figs. 4-5 accordingly) were studied in mineral separates. Mineral separation gives an opportunity to study much larger zircon grains (up to 300 μm using our separation method). However, for separated grains the mineral and textural context is lost, therefore, we can only speculate about the external sources of trace elements that could affect trace element abundances in deformed zircon domains. However, taking into account that all grains with PDBs observed in thin sections are hosted by ultramylonite and have fairly predictable position (at the contact with pseudotachylyte), we assume that separated grains had such positions as well, and were hosted by ultramylonite.

It was shown by Moser et al. (2011) that elevated temperatures are required to cause significant re-distribution of the trace elements and resetting of isotopic ages in zircon via dislocations. Planar microstructures, generated under low temperatures (“cold shock”) do not cause isotopic resetting, in contrast with the “hot shock”, where the zircon lattice was heated. This principle may also be applied to the seismic-related planar microstructures. The host rock is documented to be heated simultaneously with seismic deformation; and consistently, the re-distribution of trace elements in zircon, related to the PDBs, is observed. Zircon grains with PDBs are found in the vicinity of pseudotachylyte veins, where the elevated temperature of these frictional melts (> 1200 °C, Pittarello et al. 2008) may have facilitated observed trace element mobility in deformed zircon grains.

$^{207}Pb/^{206}Pb$ relative ages

The relative $^{207}Pb/^{206}Pb$ ages are mostly younger in domains containing PDBs (Table 1). In grain 80 (Fig. 5) relative isotopic ages, measured in lattice domains cross-cut by PDBs, are different. Upper PDB is associated with Pb-loss, whereas the lower one causes Pb-gain (Fig. 5a, white and dark-grey colored points respectively). The reason can be the gain of radiogenic Pb from the detrital core via lower PDB, which cross-cuts the core. In contrast, the PDB that cross-cuts only through metamorphic rim, causes Pb-loss, indicating Pb transfer out of the grain towards the grain boundary. However, elevated apparent age in the first case might also be due to gain of common Pb from the matrix through PDB network (e.g., Kovaleva et al. 2016). This latter speculation is difficult to prove without knowing the ^{204}Pb abundances.

It is convenient to compare relative ages in zircon fragments that were broken apart before formation of PDBs (grains 03a, 17; Figs. 6-7). PDB-free fragments show significantly older relative ages, presenting evidence of undisturbed or less disturbed Pb isotopic systems, contrasting with PDB-bearing domains that show relatively younger relative ages (Figs. 6a, 7a). Point 3 in PBD-bearing domains in grain 03b yielded significantly older relative age, probably due to proximity to the detrital core and/or the open fracture (Fig. 6a-b). We speculate that modification of Pb isotopic system may occur due to radiogenic Pb-loss, or due to gain of common Pb from the matrix, and/or radiogenic Pb from the detrital cores. Even though, without data on ^{204}Pb it is difficult to evaluate the gain of common Pb from the matrix, it seems that Pb may have become mobilized along the PDBs that have high dislocation density and thus act as fast element diffusion and/or fluid pathways (e.g., Reddy et al. 2016). Local $^{207}Pb/^{206}Pb$ ages, therefore, are younger due to out-diffusion through PDBs (grains 80, 03b, 17; Figs. 5a, points 2-5; 6a, points 4-5; 7a, points 3-5 accordingly), or older, due to inward diffusion of the radiogenic Pb though PDBs from the detrital cores (grains 80 and 03b, Figs. 5a, points 6-8; 6a, point 3 accordingly).

Pb-loss and localized resetting of the U-Pb system, connected with crystal-plastic deformation, has been previously documented by a number of authors (e.g., Nemchin et al. 2009, Moser et al. 2009, 2011; Timms et al. 2011, 2012; Piazolo et al. 2012; Grange et al. 2013; MacDonald et al. 2013). Nemchin et al. (2009) and Moser et al. (2011) documented that the domain of maximum misorientation in deformed zircon spatially coincides with the area of maximum Pb-loss and the younger apparent ages. It has been even suggested that the observed resetting of U-Pb system can potentially yield the timing of deformation (Nemchin et al. 2009; Moser et al. 2009; Peterman et al. 2016). Our observations on Pb behavior are generally consistent with the previous data and mostly show resetting of relative $^{207}Pb/^{206}Pb$ ages for zircon domains that are affected by PDBs, hence, indicate Pb-loss. It is, however, difficult to access the degree of isotopic system resetting, and to tell whether deformed domains yield the age of deformation, without analyses of U and Th.

IMPLICATIONS

The microstructural study of seismically-deformed zircon, coupled with the trace elements and radiogenic isotopes distribution study demonstrates the effect on trace elements abundances, caused by co-seismic PDBs. $^{207}Pb/^{206}Pb$ relative ages demonstrate systematic resetting of the PDB-bearing lattice domains with respect to PDB-free; and, in some cases, older relative ages, where the PDBs provide the source of radiogenic Pb from older detrital cores. Therefore, the formation of PDBs in zircon potentially has important implications for zircon U/Pb geochronology. If the isotopic ages of deformed zircon are reset, it may be possible to constrain the timing of the seismic/deformation events that produced

PDBs, or were coeval with their formation. The zircon grains with potentially reset isotopic ages and distorted microchemistry should be searched for in ultramylonites adjacent to pseudotachylyte veins, next to their contacts, where co-seismically deformed zircon grains are commonly found.

Further investigations of PDBs phenomena and other deformation microstructures, applying of U/Th/Pb absolute age dating to zircons with PDBs, careful investigation of associated microstructures should help with the reconstruction of tectono-metamorphic history of the host rocks. Furthermore, such studies show the micro-effects of seismic energy released at depth, and help to relate deep earthquakes, high-grade metamorphism and element transfer in the crust.

ACKNOWLEDGMENTS

This study was funded by the University of Vienna (doctoral school "DOGMA", project IK 052). The authors are grateful to Christian Auer, Claudia Beybel, Franz Biedermann, Sigrid Hrabe, Matthew Huber, Arno Schintlmeister and all colleagues of the FOR741 research group for fruitful discussions and the Geological Survey of Austria for access to the SEM; to Caltech Microanalyses Center, Pasadena, USA, for access to the NanoSIMS, and especially to John Eiler and Yunbin Guan, who provided the access to laboratory and assisted with data collection. The authors acknowledge access to the Laboratory for scanning electron microscopy and focused ion beam applications, Faculty of Earth Sciences, Geography and Astronomy at the University of Vienna (Austria). Gerlinde Habler assisted with the EBSD data collection and edited the manuscript. Comments of S. Reddy and N. Timms helped to improve the manuscript. We also greatly appreciate comments and suggestions of A. Cavosie and anonymous reviewer, who helped this work to get published.

REFERENCES CITED

Ashwal, L.D., Tucker, R.D., and Zinner, E.K. (1999) Slow cooling of deep crustal granulites and Pb-loss in zircon. Geochimica et Cosmochimica Acta, 63, 2839–2851.

Austrheim, H., Erambert, M., and Boundy, T.M. (1996) Garnet recording deep crustal earthquakes. Earth and Planetary Science Letters. 139, 223-238.

Austrheim, H., and Corfu, F. (2009) Formation of planar deformation features (PDFs) in zircon during coseismic faulting and an evaluation of potential effects on U–Pb systematics. Chemical Geology, 261, 25–31.

Bachmann, F., Hielscher, R., and Schaeben, H. (2010) Texture Analysis with MTEX – Free and Open Source Software Toolbox. Solid State Phenomena, 160, 63-68.

Bachmann, F., Hielscher, R., and Schaeben, H. (2011) Grain detection from 2d and 3d EBSD data-specification of the MTEX algorithm. Ultramicroscopy, 111, 1720-1733.

Bea, F., and Montero, P., 2013. Diffusion-induced disturbances of the U–Pb isotope system in pre-magmatic zircon and their influence on SIMS dating. A numerical study. Chemical Geology, 349–350, 1–17.

Bellucci, J.J, Whitehouse, M.J., Nemchin, A.A., Snape, J.F., Pidgeon, R.T., Grange, M., Reddy, S.M., and Timms, N.E. (2016) A scanning ion imaging investigation into the micron-scale U-Pb systematics in a complex lunar zircon. Chemical Geology, 438, 112-122.

Bohor, B.F., Betterton, W.J., Krogh, T.E. (1993) Impact-shocked zircons: discovery of shock-induced textures reflecting increasing degrees of shock metamorphism. Earth and Planetary Science Letters, 119, 419-424.

This is a preprint, the final version is subject to change, of the American Mineralogist (MSA)
Cite as Authors (Year) Title. American Mineralogist, in press.
(DOI will not work until issue is live.) DOI: http://dx.doi.org/10.2138/am-2017-5975

Boehnke, P., Watson, E.B., Trail, D., Harrison, T.M., and Schmitt, A.K. (2013) Zircon saturation re-revisited. Chemical Geology, 351, 324–334.

Brodie, K.H., and Rutter, E.H. (1987) Deep crustal extensional faulting in the Ivrea Zone of Northern Italy. Tectonophysics, 140, 193–212.

Brodie, K.H., Rutter, E.H., and Rex, D. (1989) On the age of deep crustal extensional faulting in the Ivrea Zone, northern Italy. Geological Society of London, Special Publications, 45, 203-210.

Brodie, K.H., Rutter, E.H., and Evans, P. (1992) On the structure of the Ivrea-Verbano Zone (northern Italy) and its implications for present-day lower continental crust geometry. Terra Nova, 4, 34-39.

Cavosie, A.J., Valley, J.W., Wilde, S.A., and E.I.M.F. (2006) Correlated microanalysis of zircon: Trace element, $\delta^{18}O$, and U–Th–Pb isotopic constraints on the igneous origin of complex >3900 Ma detrital grains. Geochimica et Cosmochimica Acta, 70, 5601–5616.

Cavosie, A.J., Quintero, R.R., Radovan, H.A., and Moser, D.E. (2010) A record of ancient cataclysm in modern sand: Shock microstructures in detrital minerals from the Vaal River, Vredefort Dome, South Africa. Geological Society of America Bulletin, 122, 1968-1980.

Cavosie, A.J., Erickson, T.M., and Timms, N.E. (2015a) Nanoscale records of ancient shock deformation: Reidite ($ZrSiO_4$) in sandstone at the Ordovician Rock Elm impact crater. Geology, 43, 315-318.

Cavosie, A.J., Erickson, T.M., Timms, N.E., Reddy, S.M., Talavera, C., Montalvo, S.D., Pincus, M.R., Gibbon, R.J., and Moser, D. (2015b) A terrestrial perspective on using *ex situ* shocked zircons to date lunar impacts. Geology, 43, 999-1002.

Cavosie, A.J., Montalvo, P.E., Timms, N.E., and Reddy, S.M. (2016) Nanoscale deformation twinning in xenotime, a new shocked mineral, from the Santa Fe impact structure (New Mexico, USA). Geology, 44, 803–806.

Cherniak, D.J., and Watson, E.B. (2000) Pb diffusion in zircon. Chemical Geology, 172, 5–24.

Cherniak, D.J., and Watson, E.B. (2003). Diffusion in Zircon. In J.M. Hanchar and P.W.O. Hoskin, Eds., Zircon, 53, p. 113-143. Reviews in Mineralogy and Geochemistry, Mineralogical Society of America, Chantilly, Virginia.

Cherniak, D.J., and Watson, E.B. (2007) Ti diffusion in zircon. Chemical Geology, 242, 470–483.

Cherniak, D.J., Lanford, W.A., and Ryerson, F.J. (1991) Lead diffusion in apatite and zircon using ion implantation and Rutherford Backscattering techniques. Geochimica et Cosmochimica Acta, 55, 1663-1673.

Cherniak, D.J., Hanchar, J.M., Watson, and E.B. (1997a) Rare earth diffusion in zircon. Chemical Geology, 134, 289–301.

Cherniak, D.J., Hanchar, J.M., and Watson, E.B. (1997b) Diffusion of tetravalent cations in zircon. Contributions to Mineralogy and Petrology, 127, 383–390.

Compston, W., Kinny, P.D., Williams I.S., and Foster J.J. (1986) The age and Pb loss behaviour of zircons from the Isua supracrustal belt as determined by ion microprobe. Earth and Planetary Science Letters, 80, 71-81.

Corfu, F., Hanchar, J.M., Hoskin, P.W.O., and Kinny, P. (2003) Atlas of zircon textures. In J.M. Hanchar and P.W.O. Hoskin, Eds., Zircon, 53, p. 468–500. Reviews in Mineralogy and Geochemistry, Mineralogical Society of America, Chantilly, Virginia.

Davis, D.W., Williams, I.S., and Krogh, T.E. (2003) Historical development of zircon geochronology. In J.M. Hanchar and P.W.O. Hoskin, Eds., Zircon, 53, p. 145-181. Reviews in Mineralogy and Geochemistry, Mineralogical Society of America, Chantilly, Virginia.

Erdmann, S., Wodicka, N., Jackson, S.E., and Corrigan, D. (2013) Zircon textures and composition: refractory recorders of magmatic volatile evolution? Contributions to Mineralogy and Petrology, 165, 45–71.

Erickson, T.M., Cavosie, A.J., Moser, D.E., Barker, I.R., and Radovan, H.A. (2013a) Correlating planar microstructures in shocked zircon from the Vredefort Dome at multiple scales: Crystallographic modeling, external & internal imaging, and EBSD structural analysis. American Mineralogist, 98, 53-65.

Erickson, T.M., Cavosie, A.J., Moser, D.E, Barker, I.R., Radovan, H.A., and Wooden, J. (2013b) Identification and provenance determination of distally transported, Vredefort-derived shocked minerals in the Vaal River, South Africa using SEM and SHRIMP-RG techniques. Geochimica et Cosmochimica Acta, 107, 170-188.

Ferry, J., and Watson, E.B. (2007) New thermodynamic models and revised calibrations for the Ti-in-zircon and Zr-in-rutile thermometers. Contributions to Mineralogy and Petrology, 154, 429-437.

Flowers, R.M., Schmitt, A.K., and Grove, M. (2010) Decoupling of U–Pb dates from chemical and crystallographic domains in granulite facies zircon. Chemical Geology, 270, 20–30.

Frei, D., and Gerdes, A. (2009) Precise and accurate in situ U–Pb dating of zircon with high sample throughput by automated LA-SF-ICP-MS. Chemical Geology, 261, 261–270.

Geisler, T., Ulonska, M., Schleicher, H., Pidgeon, R.T., and Van Bronswijk, W. (2001) Leaching and differential recrystallization of metamict zircon under experimental hydrothermal conditions. Contributions to Mineralogy and Petrology, 141, 53–65.

Geisler, T., Pidgeon, R.T., Bronswijk, W., and Kurtz, R. (2002) Transport of uranium, thorium, and lead in metamict zircon under low-temperature hydrothermal conditions. Chemical Geology, 191, 141–154.

Geisler, T., Pidgeon, R.T., Kurtz, R., Bronswijk, W., and Schleicher H. (2003) Experimental hydrothermal alteration of partially metamict zircon. American Mineralogist, 88, 1496-1513.

Grange, M.L., Pidgeon, R.T., Nemchin, A.A., Timms, N.E., and Meyer, C. (2013) Interpreting U–Pb data from primary and secondary features in lunar zircon. Geochimica et Cosmochimica Acta, 101, 112–132.

Halpin, J.A., Daczko, N.R., Milan, L.A., and Clarke, G.L. (2012) Decoding near-concordant U–Pb zircon ages spanning several hundred million years: recrystallisation, metamictisation or diffusion? Contributions to Mineralogy and Petrology, 163, 67–85.

Hanchar, J.M., Finch, R.J., Hoskin, P.W.O., Watson, E.B., Cherniak, D.J., and Mariano, A.N. (2001) Rare earth elements in synthetic zircon: Part 1. Synthesis, and rare earth element and phosphorus doping. American Mineralogist, 86, 667-680.

Harrison, T.M., and Schmitt, A.K. (2007) High sensitivity mapping of Ti distributions in Hadean zircons. Earth and Planetary Science Letters, 261, 9–19.

Hofmann, A.E., Valley, J.W., Watson, E.B., Cavosie, A.J., and Eiler, J.M. (2009) Sub-micron scale distributions of trace elements in zircon. Contributions to Mineralogy and Petrology, 158, 317–335.

Hofmann, A.E., Backer, B.M., and Eiler, J.M. (2014) Sub-micron-scale trace-element distributions in natural zircons of known provenance: implications for Ti-in-zircon thermometry. Contributions to Mineralogy and Petrology, 168, 1057. doi: 10.1007/s00410-014-1057-8

Hoskin, P.W.O., and Schaltegger, U. (2003) The Composition of Zircon and Igneous and Metamorphic Petrogenesis. In J.M. Hanchar and P.W.O. Hoskin, Eds., Zircon, 53, p. 27-62. Reviews in Mineralogy and Geochemistry, Mineralogical Society of America, Chantilly, Virginia.

Kalleson, E., Corfu, F., and Dypvik, H. (2009) U–Pb systematics of zircon and titanite from the Gardnos impact structure, Norway: Evidence for impact at 546 Ma? Geochimica et Cosmochimica Acta, 73, 3077–3092.

Kamo, S.L., Reimold, W.U., Krogh, T.E., and Colliston, W.P. (1996) A 2.023 Ga age for the Vredefort impact event and a first report of shock metamorphosed zircons in pseudotachylitic breccias and granophyre. Earth and Planetary Science Letters, 144, 369–387.

Klötzli, U.S., Sinigoi, S., Quick, J.E., Demarchi, G., Tassinari, C.C.G., Sato, K., and Günes, Z. (2014) Duration of igneous activity in the Sesia Magmatic System and implications for high-temperature metamorphism in the Ivrea–Verbano deep crust. Lithos, 206–207, 19–33.

Kovaleva, E., Klötzli, U., Habler, G., and Libowitzky, E. (2014) Finite lattice distortion patterns in plastically deformed zircon grains. Solid Earth, 5, 1099-1122.

Kovaleva, E., Klötzli, U., Habler, G., and Wheeler, J. (2015) Planar microstructures in zircon from paleo-seismic zones. American Mineralogist, 100, 1834-1847.

Kovaleva, E., Klötzli, U., Habler, G., Huet, B., Guan, Y., and Rhede, D. (2016) The effect of crystal-plastic deformation on isotope and trace element distribution in zircon: Combined BSE, CL, EBSD, FEG-EMPA and NanoSIMS study. Chemical Geology, in press.

Kusiak, M.A., Dunkley, D.J., Słaby, E., Martin, H, and Budzyn, B. (2009) Sensitive high-resolution ion microprobe analysis of zircon reequilibrated by late magmatic fluids in a hybridized pluton. Geology, 37, 1063–1066.

Kusiak, M.A., Whitehouse, M.J., Wilde, S.A., Dunkley, D.J., Menneken, M., Nemchin, A.A., and Clark, C. (2013) Changes in zircon chemistry during Archean UHT metamorphism in the Napier Complex, Antarctica. American Journal of Science, 313, 933–967.

Kusiak, M.A., Dunkley, D.J., Wirth, R., Whitehouse, M.J., Wilde, S.A., and Marquardt, K. (2015) Metallic lead nanospheres discovered in ancient zircons. Proceedings of the Polish National Academy of Sciences, 112, 4958-4963.

Leroux, H., Reimold, W.U., Koeberl, C., Hornemann, U., and Doukhan, J.C. (1999) Experimental shock deformation in zircon: a transmission electron microscopic study. Earth and Planetary Science Letters, 169, 291–301.

MacDonald, J.M., Wheeler, J., Harley, S.L., Mariani, E., Goodenough, K.M., Crowley, Q., and Tatham, D. (2013) Lattice distortion in a zircon population and its effects on trace element mobility and U–Th–Pb isotope systematics: examples from the Lewisian Gneiss Complex, northwest Scotland. Contributions to Mineralogy and Petrology, 166, 21–41.

Mainprice, D., Hielscher, R., and Schaeben, H. (2011) Calculating anisotropic physical properties from texture data using the MTEX open source package. Geological Society of London, Special Publications, 360, 175-192.

Moser, D.E., Davis, W.J., Reddy, S.M., Flemming, R.L., and Hart, R.J. (2009) Zircon U–Pb strain chronometry reveals deep impact-triggered flow. Earth and Planetary Science Letters, 277, 73–79.

Moser, D.E., Cupelli, C.L., Barker, I.R., Flowers, R.M., Bowman, J.R., Wooden, J., and Hart, J.R. (2011) New zircon shock phenomena and their use for dating and reconstruction of large impact structures revealed by electron nanobeam (EBSD, CL, EDS) and isotopic U–Pb and (U–Th)/He analysis of the Vredefort dome. Canadian Journal of Earth Sciences, 48, 117–139.

Nasdala, L., Hanchar, J. M., Rhede, D., Kennedy, A. K., and Vaczi, T. (2010) Retention of uranium in complexly altered zircon: an example from Bancroft, Ontario. Chemical Geology, 269, 290-300.

Nemchin, A., Timms, N.E., Pidgeon, R., Geisler, T., Reddy, S.M., and Meyer, C. (2009) Timing of crystallization of the lunar magma ocean constrained by the oldest zircon. Nature Geoscience, 2, 133-136.

Peterman, E.M., Reddy, S.M., Saxey, D.W., Snoeyenbos, D.R., Rickard, W.D.A., Fougerouse, D., and Kylander-Clark, R.A.C. (2016). Nanogeochronology of discordant zircon measured by atom probe microscopy of Pb-enriched dislocation loops. Science Advances, 2, e1601318.

Piazolo, S., Austrheim, H., and Whitehouse, M. (2012) Brittle-ductile microfabrics in naturally deformed zircon: Deformation mechanisms and consequences for U-Pb dating. American Mineralogist, 97, 1544–1563.

Piazolo, S., La Fontaine, A., Trimby, P., Harley, S., Yang, L., Armstrong, R., and Cairney, J.M. (2016) Deformation-induced trace element redistribution in zircon revealed using atom probe tomography. Nature Communication, 7, 10490.

Pittarello, L., Di Toro, G., Bizzarri, A., Pennacchioni, G., Hadizadeh, J., and Cocco, M. (2008) Energy partitioning during seismic slip in pseudotachylyte-bearing faults (Gole Larghe Fault, Adamello, Italy). Earth and Planetary Science Letters, 269, 131–139.

Pittarello, L., Pennacchioni, G., Di Toro, G. (2012) Amphibolite-facies pseudotachylytes in Premosello metagabbro and felsic mylonites (Ivrea Zone, Italy). Tectonophysics, 580, 43–57.

Polerecky, L., Adam, B., Milucka, J., Musat, N., Vagner, T., and Kuypers, M.M. (2012) Look@NanoSIMS – a tool for the analysis of nanoSIMS data in environmental microbiology. Environmental Microbiology, 14, 1009–1023.

Quick, J.E., Sinigoi, S., Peressini, G., Demarchi, G., Wooden, J.L., and Sbisà, A. (2009) Magmatic plumbing of a large Permian caldera exposed to a depth of 25 km. Geology, 37, 603-606.

Reddy, S.M., Timms, N.E., Trimby, P., Kinny, P.D., Buchan, C., and Blake, K. (2006) Crystal-plastic deformation of zircon: a defect in the assumption of chemical robustness. Geology, 34, 257-260.

Reddy, S.M., Timms, N.E., Hamilton, P.J., and Smyth, H.R. (2009) Deformation-related microstructures in magmatic zircon and implications for diffusion. Contributions to Mineralogy and Petrology, 157, 231–244.

Reddy, S.M., Johnson, T.E., Fischer, S., Rickard, W.D.A., and Taylor, R.J.M. (2015) Precambrian reidite discovered in shocked zircon from the Stac Fada impactite, Scotland. Geology, 43, 899-902.

Reddy, S.M., van Riessen, A., Saxey, D.W., Johnson, T.E., Rickard, W.D.A., Fougerouse, D., Fischer, S., Prosa, T.J., Rice, K.P., Reinhard, D.A., Chen, Y., and Olson, D. (2016) Mechanisms of deformation-induced trace element migration in zircon resolved by atom probe and correlative microscopy. Geochimica et Cosmochimica Acta, 195, 158-170.

Redler, C., Johnson, T.E., White, R.W., and Kunz, B.E. (2012) Phase equilibrium constraints on a deep crustal metamorphic field gradient: metapelitic rocks from the Ivrea Zone (NW Italy). Journal of Metamorphic Geology, 30, 235–254.

Rimsa, A., Whitehouse, M.J., Johansson, L., and Piazolo, S. (2007) Brittle fracturing and fracture healing of zircon: An integrated cathodoluminescence, EBSD, U-Th-Pb, and REE study. American Mineralogist, 92, 1213-1224.

Rutter, E.H., Brodie, K.H., James, T., and Burlini, L. (2007) Large-scale folding in the upper part of the Ivrea-Verbano zone, NW Italy. Journal of Structural Geology, 29, 1-17.

Sinigoi, S., Quick, J.E., Demarchi, G., and Klötzli, U. (2011) The role of crustal fertility in the generation of large silicic magmatic systems triggered by intrusion of mantle magma in the deep crust. Contributions to Mineralogy and Petrology, 162, 691-707.

Sláma, J., Košler, J., Condon, D.J., Crowley, J.L., Gerdes, A., Hanchar, J.M., Horstwood, M.S.A., Morris, G.A., Nasdala, L., Norberg, N., Schaltegger, U., Schoene, B., Tubrett, M.N., and Whitehouse, M.J. (2008) Plešovice zircon — A new natural reference material for U–Pb and Hf isotopic microanalysis. Chemical Geology, 249, 1–35.

Storm, S., Schmitt, A.K., Shane, P., and Lindsay, J.M. (2014) Zircon trace element chemistry at sub-micrometer resolution for Tarawera volcano, New Zealand, and implications for rhyolite magma evolution. Contributions to Mineralogy and Petrology, 167, 1000. doi: 10.1007/s00410-014-1000-z

Techmer, K.S., Ahrendt, H., and Weber, K. (1992) The development of pseudotachylyte in the Ivrea-Verbano Zone of the Italian Alps. Tectonophysics, 204, 307–322.

Thomson, O.A., Cavosie, A.J., Moser, D.E., Barker, I., Radovan, H.A., and French, B.M. (2014) Preservation of detrital shocked minerals derived from the 1.85 Ga Sudbury impact structure in modern alluvium and Holocene glacial deposits. Geological Society of America Bulletin, 126, 720-737.

Timms, N.E., Kinny, P., and Reddy, S.M. (2006) Enhanced diffusion of uranium and thorium linked to crystal plasticity in zircon. Geochemical Transactions, 7, 10. doi: 10.1186/1467-4866-7-10

Timms, N.E., Kinny, P., Reddy, S.M., Evans, K., Clark, C., and Healy, D. (2011) Relationship among titanium, rare earth elements, U–Pb ages and deformation microstructures in zircon: Implications for Ti-in-zircon thermometry. Chemical Geology, 280, 33–46.

Timms, N.E., Reddy, S.M., Healy, D., Nemchin, A.A., Grange, M.L., Pidgeon, R.T., and Hart, R. (2012) Resolution of impact-related microstructures in lunar zircon: A shock-deformation mechanism map. Meteoritics and Planetary Science, 47, 120–141.

Valley, J.W., Cavosie, A.J., Ushikubo, T., Reinhard, D.A., Lawrence, D.F., Larson, D.J., Clifton, P.H., Kelly, T.F., Wilde, S.A., Moser, D.E., and Spicuzza, M.J. (2014) Hadean age for a post-magma-ocean zircon confirmed by atom-probe tomography. Nature Geoscience, 7, 219-223.

Watson, E.B., and Liang, Y. (1995) A simple model for sector zoning in slowly grown crystals: Implications for growth rate and lattice diffusion, with emphasis on accessory minerals in crustal rocks. American Mineralogist, 80, 1179-1187.

Watson, E.B., Wark, D.A., and Thomas, J.B. (2006) Crystallization thermometers for zircon and rutile. Contributions to Mineralogy and Petrology, 151, 413–433.

Figure captions

Figure 1. Grain 12: **(a)** Orientation contrast image; directions of PDBs are shown by the white dotted lines; black frame indicates the area where EBSD map shown in (c) was collected; white arrows are pointing to the traces of healed fractures. **(b)** CL image, white arrows are pointing to the traces of healed fractures. **(c)** EBSD cumulative misorientation map of the area highlighted in (a), misorientation is color coded with respect to a user-selected reference point (white star). Black arrows point to the intersection sites of orthogonal PDBs with elevated misorientation. **(d)** Pole figure for the area of EBSD map, color coding correspond to EBSD map shown in (c). Disorientation axis [331] is highlighted by a small black circle; black lines indicate the direction of PDBs, red dotted lines are the reconstruction of PDBs crystallographic orientation. Labels in square brackets indicate the positions of crystallographic axes. **(e)** Inverse pole figure with density contours of orientations of misorientation axes.

Figure 2. Grain 26: **(a)** Orientation contrast image; black frame indicates the area where EBSD map shown in (c) was collected; white frame indicates the area where ion maps shown in (e) were collected; direction of PDBs is shown by the white dotted line. White arrow points to the PDB in the offset fragment. **(b)** CL image; white frame indicates the area

where ion maps shown in (e) were collected. **(c)** EBSD cumulative misorientation map, misorientation is color coded with respect to a user-selected reference point (white star), location of EBSD map marked in (a). Grey regions indicate the areas with the misorientation higher than 3° with respect to a reference point and thus not color-coded. White frame indicates the area where ion maps shown in (e) were collected. White dotted line indicates the direction of PDBs, black arrows point to the subparallel low angle boundaries, orthogonal to PDBs. **(d)** Pole figure, color coding corresponds to EBSD map shown in (c); black lines indicate the direction of (sub)planar deformation features, red dotted lines are the reconstruction of their crystallographic orientation. Labels in square brackets indicate the positions of crystallographic axes. **(e)** Ion maps; white frame with lines indicates orientation of the deformation features over this area; same lines in the Pb map: solid line corresponds to the fracture, dotted lines indicate positions of the discrete planar bands. Arrows point to “patchy” enrichments in radiogenic Pb isotopes. Maps are 10x10 μm in size, location marked in (a) and (b), intensity in counts per second normalized to ^{180}Hf.

Figure 3. Grain 43: **(a)** Orientation contrast image; directions of the PDBs are shown by the white dotted lines. White frame indicates the area where ion maps shown in (c) were collected. EBSD map is overlaying, misorientation is color-coded with respect to a reference point marked by a white marker. **(b)** CL image. White frame as in (a). **(c)** Ion maps; white frame with lines indicates orientation of the deformation and growth features over this area: dashed line indicates the position of CL intensity gradient between CL-dark rim and CL-bright core, dotted lines indicate the positions of the PDBs cross-cutting analyzed area, circle indicates the position of enrichment in Pb isotopes. Arrows point to local enrichments in Pb isotopes. Ion maps are 15x15 μm in size, location marked in (a) and (b), intensity in counts per second normalized to ^{180}Hf.

Figure 4. Grain 91: **(a)** Orientation contrast image, direction of the PDBs and PFs is shown by a white dotted line. Inset shows the analyzed area enlarged. **(b)** CL image, white frame in (a) and (b) indicates the area where ion maps were collected (inset shows this area enlarged), and white arrows point to the trace of healed fracture resolved by ion mapping. **(c)** Ion maps; white frame with lines indicates orientation of the deformation and growth features over this area: solid line indicates the position of healed fracture, dashed lines indicate the position of boundary between growth zones, dotted lines indicate the positions of PDBs cross-cutting this area. White arrows point to the inhomogeneities in trace element abundances caused by healed fracture. Maps are 20x20 µm in size, location marked in (a) and (b), intensity in counts per second normalized to ^{90}Zr.

Figure 5. Grain 80: **(a)** Orientation contrast image with locations of NanoSIMS point analyses, spot size <1x1 µ (see analytical data section), points color-coded according to the $^{207}Pb/^{206}Pb$ relative ages; direction of the PDBs is highlighted by a white dotted line. EBSD map is overlaying; misorientation is color-coded with respect to a reference point marked by a white marker. **(b)** CL image with locations of analyses. Dotted lines indicate the positions of PDBs, which are cross-cut by the microprobe profile. **(c)** Pole figure corresponding to EBSD map shown in (a); white lines indicate the direction of PDBs, red dotted line is the reconstruction of the PDBs crystallographic orientation. **(d)** Microprobe profiles along the points 1-9 marked in (a)-(b), gray boxes highlight the points along the profile, which spatially coincide with PDBs. Error bars represent uncertainties (σ_{mean}).

Figure 6. Grain 03b: **(a)** Orientation contrast image with locations of analyses, spot size is <2x2 µm, points color-coded according to the $^{207}Pb/^{206}Pb$ relative ages; directions of the PDBs are shown by white dotted lines. Local misorientation EBSD map is overlaying, misorientation of each pixel is color-coded with respect to the neighboring pixels. **(b)** CL

image with locations of analyses. **(c)** Ion microprobe analyses, gray box highlights the results obtained in PDB-bearing fragment. Error bars represent uncertainties (σ_{mean}).

Figure 7. Grain 17: **(a)** Orientation contrast image with locations of microprobe analyses, spot size is <2x2 μm, points color-coded according to the $^{207}Pb/^{206}Pb$ relative ages; direction of the PDBs is indicated by a white dotted line. **(b)** CL image with locations of point analyses. White arrows in (a) and (b) point to the trace of healed fracture. **(c)** Ion microprobe analyses, gray box highlights the results obtained in PDB-bearing fragment. Error bars represent uncertainties (σ_{mean}).

Figure 1

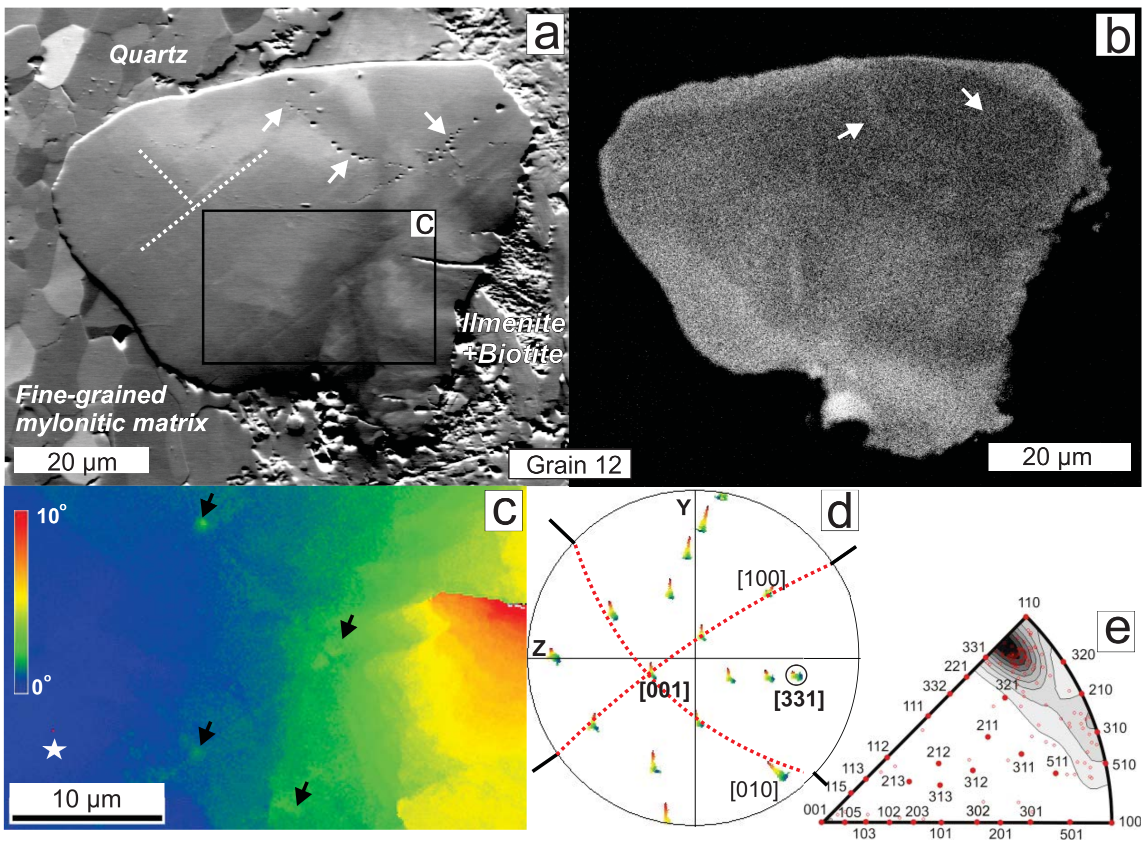
a
Quartz
c
Ilmenite
+Biotite
Fine-grained
mylonitic matrix
20 µm
Grain 12
b
20 µm
c
10°
0°
10 µm
d
Y
Z
[100]
[001]
[331]
[010]
e
110
331
320
221
321
210
332
111
211
310
112
212
311
511
510
113
213
312
115
313
001
105
102
203
302
301
100
103
101
201
501

Figure 2

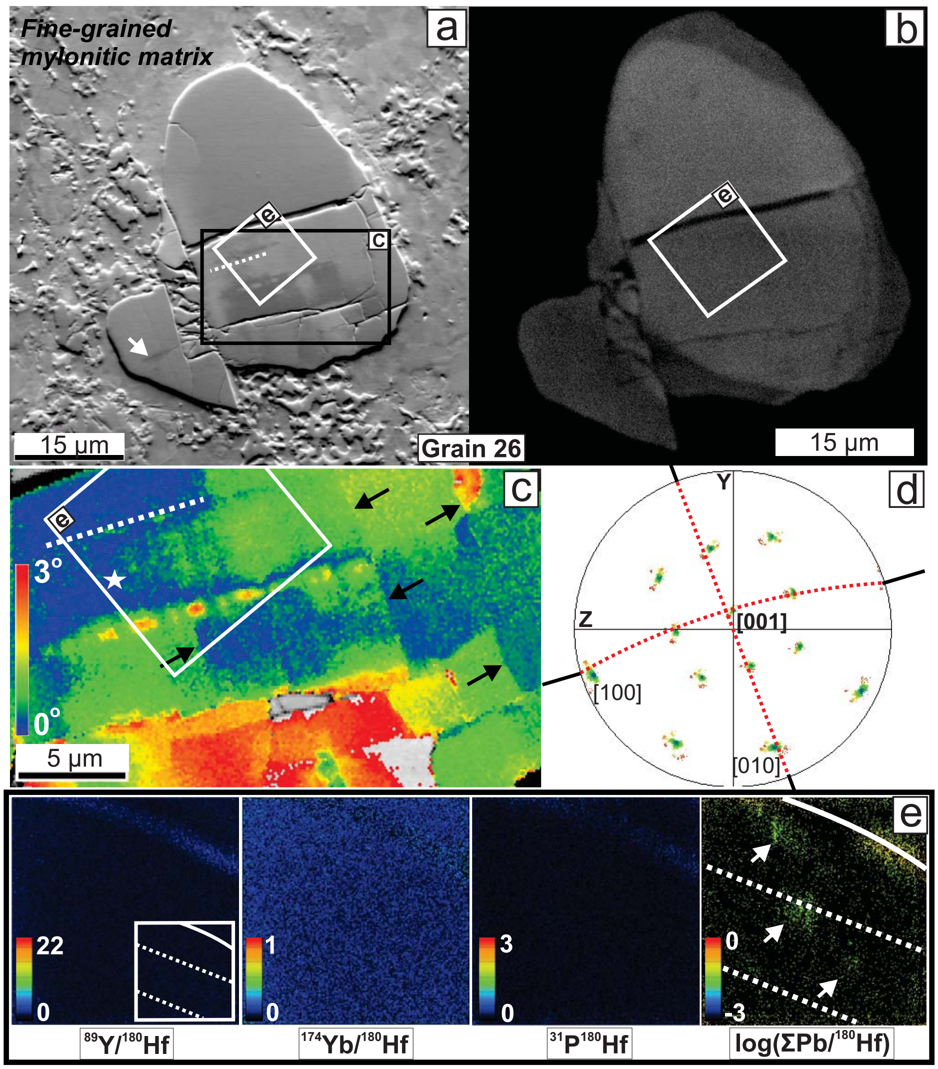
a
Fine-grained
mylonitic matrix
e
c
15 µm
Grain 26
b
e
15 µm
c
e
3°
0°
5 µm
d
Y
Z
[001]
[100]
[010]
e
22
0
1
0
3
0
0
-3
⁸⁹Y/¹⁸⁰Hf
¹⁷⁴Yb/¹⁸⁰Hf
³¹P¹⁸⁰Hf
log(ΣPb/¹⁸⁰Hf)

This is a preprint, the final version is subject to change, of the American Mineralogist (MSA)
Cite as Authors (Year) Title. American Mineralogist, in press.
(DOI will not work until issue is live.) DOI: http://dx.doi.org/10.2138/am-2017-5975

Figure 3

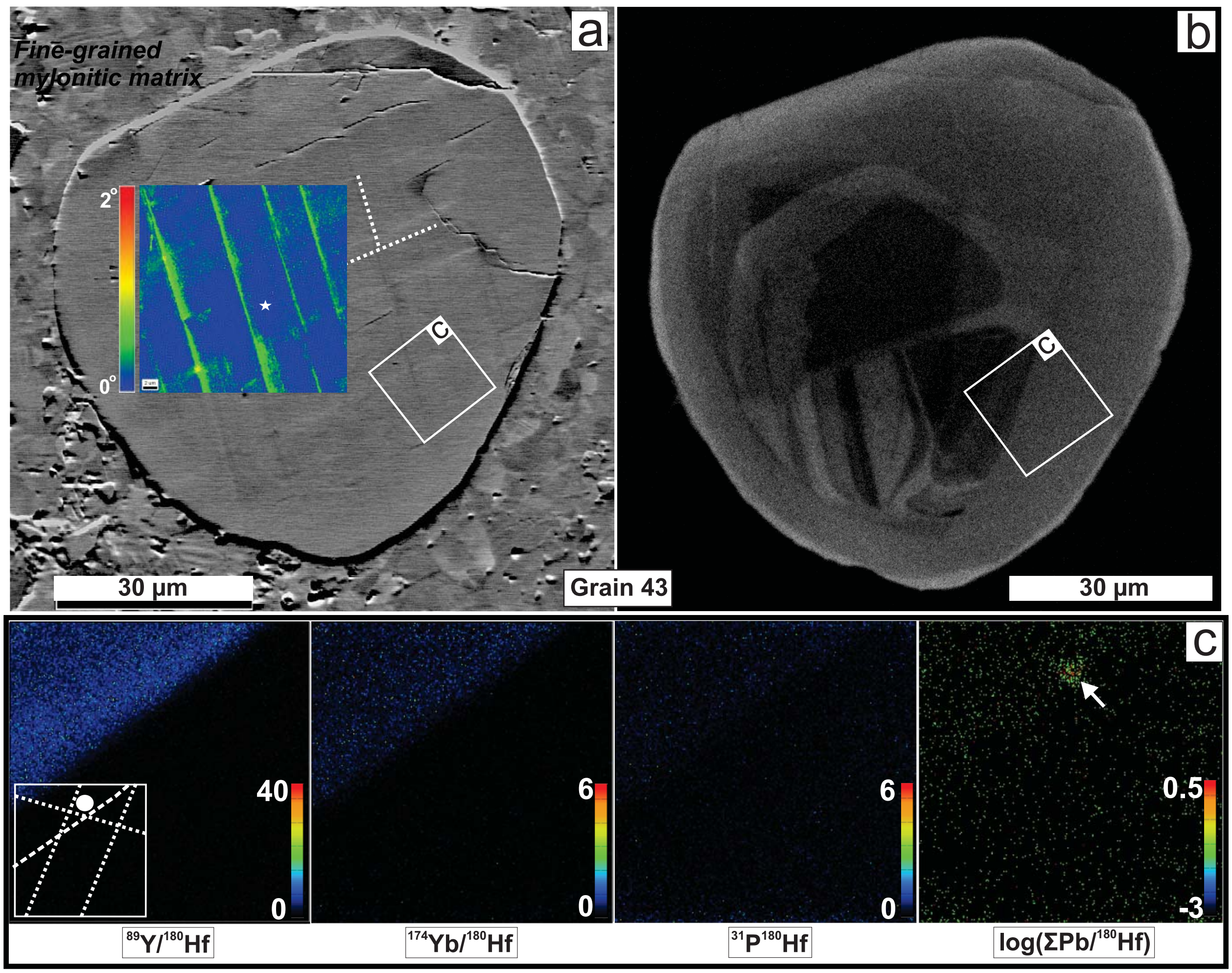

This is a preprint, the final version is subject to change, of the American Mineralogist (MSA)
Cite as Authors (Year) Title. American Mineralogist, in press.
(DOI will not work until issue is live.) DOI: http://dx.doi.org/10.2138/am-2017-5975

Figure 4

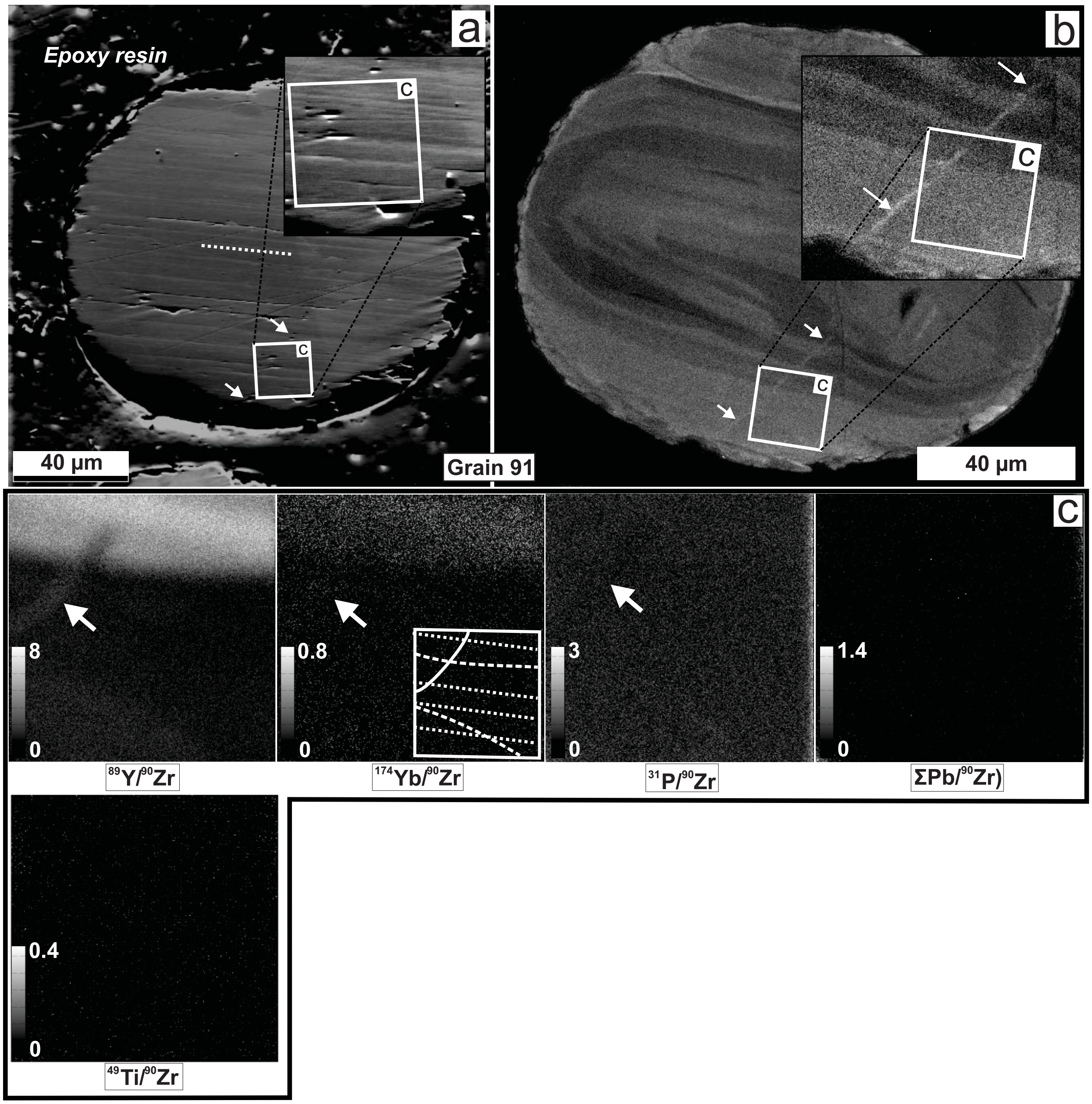

Figure 5

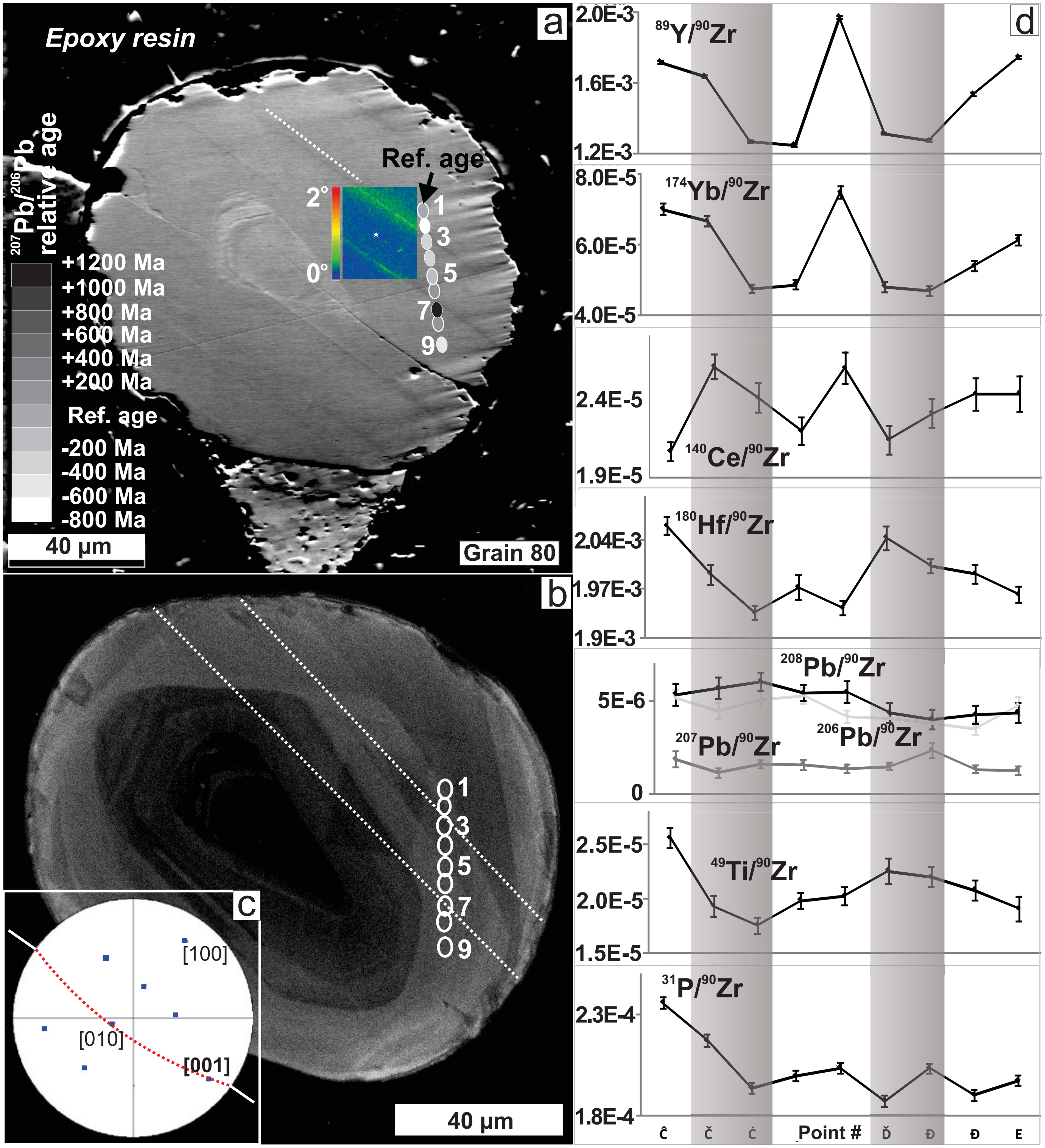
a
Epoxy resin
207Pb/206Pb relative age
+1200 Ma
+1000 Ma
+800 Ma
+600 Ma
+400 Ma
+200 Ma
Ref. age
-200 Ma
-400 Ma
-600 Ma
-800 Ma
40 µm
Ref. age
2°
0°
1
3
5
7
9
Grain 80
b
1
3
5
7
9
40 µm
c
[100]
[010]
[001]
d
89Y/90Zr
2.0E-3
1.6E-3
1.2E-3
174Yb/90Zr
8.0E-5
6.0E-5
4.0E-5
140Ce/90Zr
2.4E-5
1.9E-5
180Hf/90Zr
2.04E-3
1.97E-3
1.9E-3
208Pb/90Zr
206Pb/90Zr
207Pb/90Zr
5E-6
0
49Ti/90Zr
2.5E-5
2.0E-5
1.5E-5
31P/90Zr
2.3E-4
1.8E-4
Point #

This is a preprint, the final version is subject to change, of the American Mineralogist (MSA)
Cite as Authors (Year) Title. American Mineralogist, in press.
(DOI will not work until issue is live.) DOI: http://dx.doi.org/10.2138/am-2017-5975

Figure 6

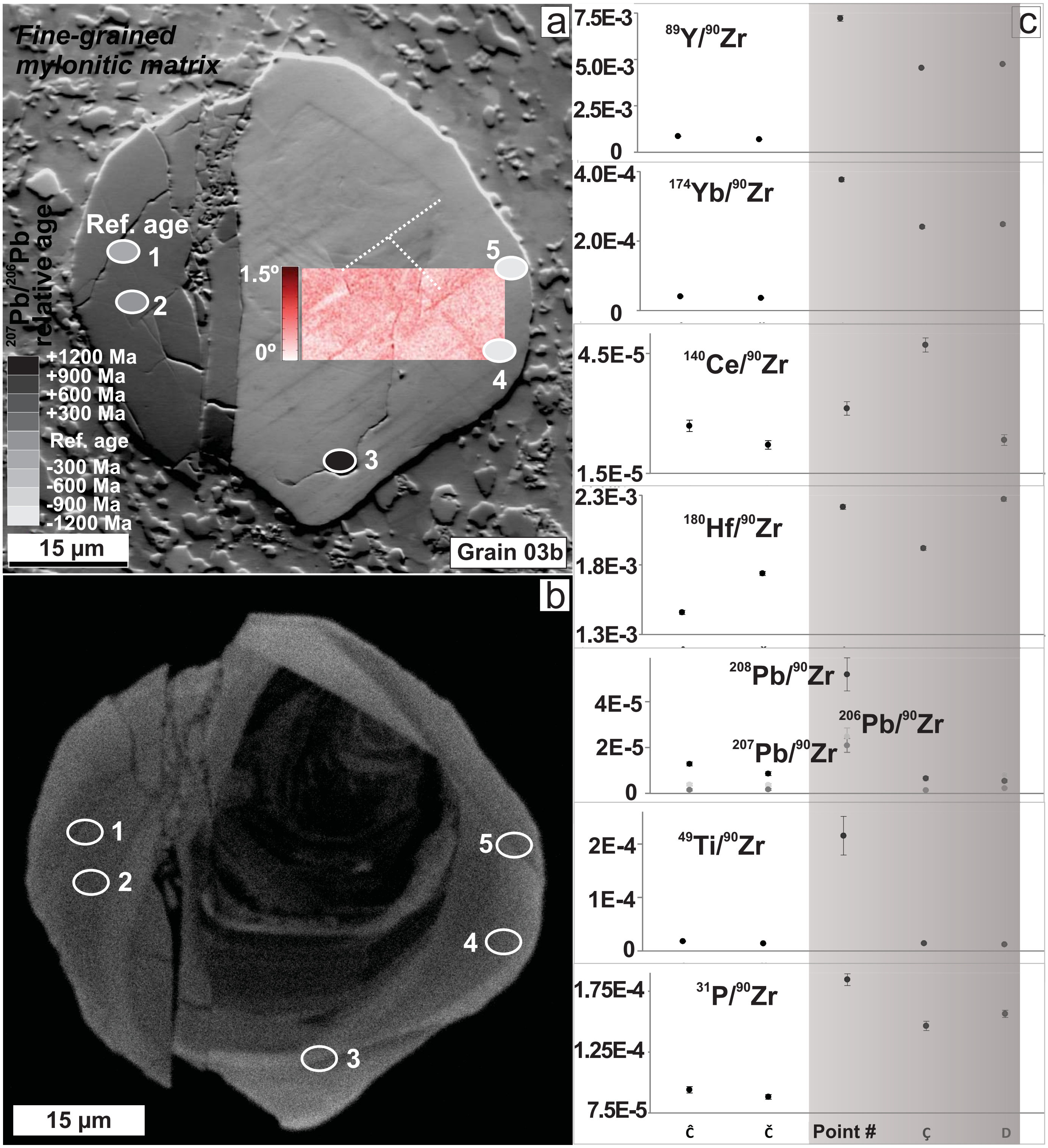

Figure 7

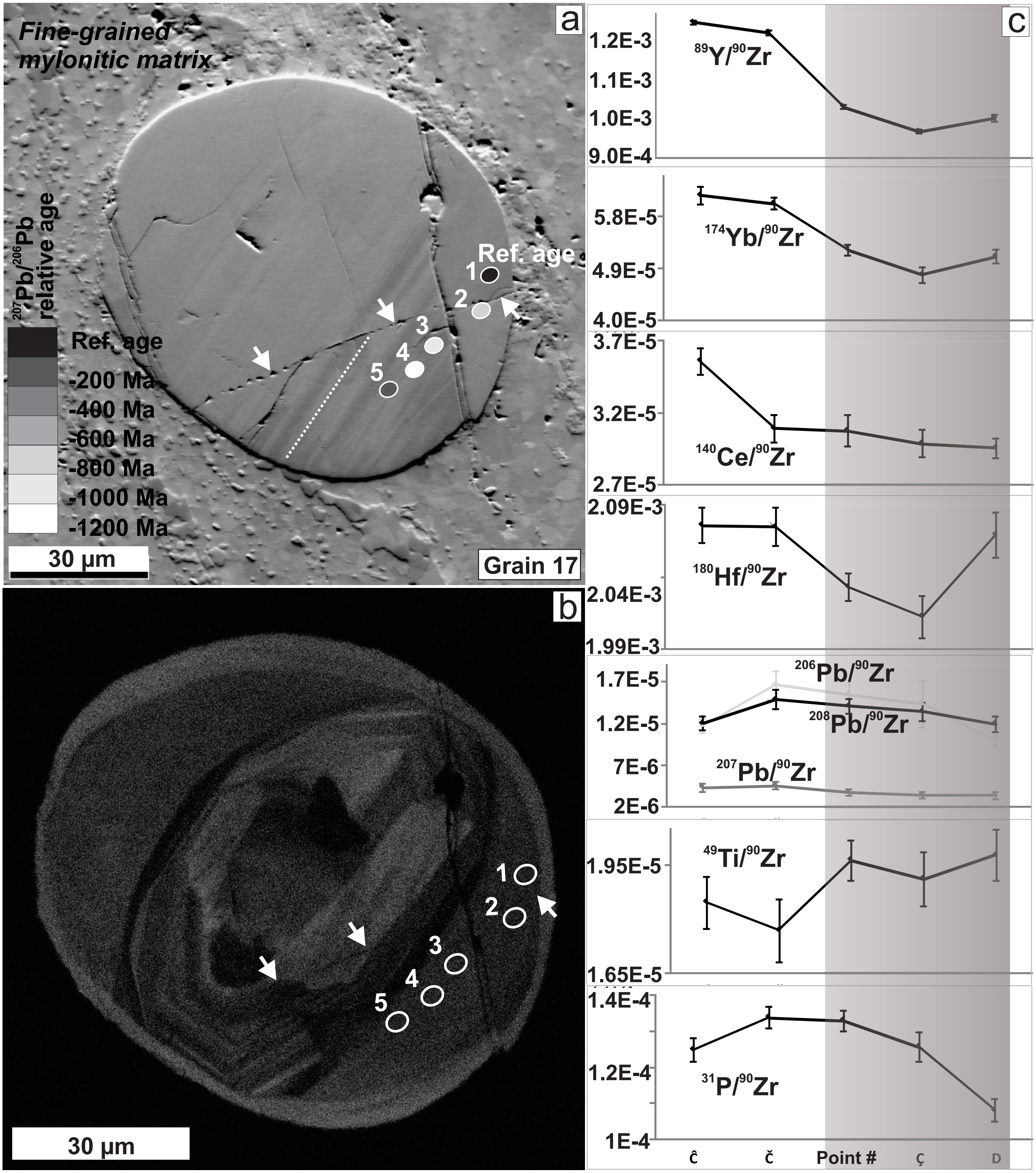
a
Fine-grained mylonitic matrix
207Pb/206Pb relative age
Ref. age
-200 Ma
-400 Ma
-600 Ma
-800 Ma
-1000 Ma
-1200 Ma
30 µm
Grain 17
Ref. age
1
2
3
4
5
b
30 µm
c
1.2E-3
1.1E-3
1.0E-3
9.0E-4
89Y/90Zr
5.8E-5
4.9E-5
4.0E-5
174Yb/90Zr
3.7E-5
3.2E-5
2.7E-5
140Ce/90Zr
2.09E-3
2.04E-3
1.99E-3
180Hf/90Zr
1.7E-5
1.2E-5
7E-6
2E-6
206Pb/90Zr
208Pb/90Zr
207Pb/90Zr
1.95E-5
1.65E-5
49Ti/90Zr
1.4E-4
1.2E-4
1E-4
31P/90Zr
Point #

Point N	$^{207}Pb/^{206}Pb$	$^{207}Pb/^{206}Pb$ age, Ma
Grain 80 (Fig. 7)		
1 (ref.)	0.0680	869
2	0.0491	153
3	0.0613	649
4	0.0565	471
5	0.0629	703
6	0.0695	915
7	0.1195	1949
8	0.0720	985
9	0.0519	283
Grain 03b (Fig. 8)		
1 (ref.)	0.0693	907
2	0.0784	1156
3	0.1558	2410
4	0.0479	93
5	0.0476	78
Grain 17 (Fig. 9)		
1 (ref.)	0.0844	1303
2	0.0600	606
3	0.0549	410
4	0.0519	284
5	0.0777	1141

Table 1. $^{207}Pb/^{206}Pb$ ratios corrected with the correction factor 1.016. Relative $^{207}Pb/^{206}Pb$ ages are calculated with Excel toolbox Isoplot 4.15. Ref. – user-selected reference age.